Evaluation of natural aerosols in CRESCENDO-ESMs: Mineral Dust

Ramiro Checa-Garcia[1], Yves Balkanski[1], Samuel Albani[8], Tommi Bergman[5], Ken Carslaw[2], Anne Cozic[1], Chris Dearden[10], Beatrice Marticorena[3], Martine Michou[4], Twan van Noije[5], Pierre Nabat[4], Fionna O'Connor[7], Dirk Olivié[6], Joseph M. Prospero[9], Philippe Le Sager[5], Michael Schulz[6], and Catherine Scott[2]

[1]Laboratoire des Sciences du Climat et de l'Environnement, CEA-CNRS-UVSQ, IPSL, Gif-sur-Yvette, France
[2]Institute for Climate & Atmospheric Science, School of Earth & Environment, University of Leeds, United Kingdom
[3]LISA, Universités Est-Paris & Diderot-Paris, France
[4]CNRM, Université de Toulouse, Météo-France, CNRS, Toulouse, France
[5]Royal Netherlands Meteorological Institute, De Bilt, Netherlands
[6]Norwegian Meteorological Institute, Oslo, Norway
[7]Met Office Hadley Centre in Exeter, United Kingdom
[8]Department of Environmental & Earth Sciences, University of Milano-Bicocca, Italy
[9]Department of Atmospheric Sciences, University of Miami, USA
[10]Centre for Environmental Modelling & Computation (CEMAC), School of Earth & Environment, University of Leeds, UK

Correspondence: Ramiro Checa-Garcia (ramiro.checa-garcia@lsce.ipsl.fr)

Abstract.

This paper presents an analysis of the mineral dust aerosol modelled by five Earth System Models (ESM) within the Coordinated Research in Earth Systems and Climate: Experiments, kNowledge, Dissemination and Outreach (CRESCENDO) project. We quantify the global dust cycle described

5 by each model in terms of global emissions together with dry and wet depositions, reporting large differences in ratio of dry over wet deposition across the models not directly correlated with the range of particle sizes emitted. The multi-model mean dust emissions was 2954 $\mathrm{Tg\,yr^{-1}}$ but with a large uncertainty due mainly to the difference in maximum dust particle size emitted. For the subset of ESMs without particles larger than 10 µm we obtained 1664 (σ=650) $\mathrm{Tg\,yr^{-1}}$. Total dust

10 emissions with identical nudged winds from reanalysis give us better consistency between models with 1530 (σ=282) $\mathrm{Tg\,yr^{-1}}$. Significant discrepancies in the globally averaged dust mass extinction efficiency explain why even models with relatively similar dust load global budgets can display strong differences in dust optical depths. The comparison against observations has been done in terms of dust optical depths based on MODIS satellite products, showing a global consistency in

15 terms of preferential dust sources and transport across the Atlantic. However, we found regional

and seasonal differences between models and observations when we quantified the cross-correlation of time-series over dust emitting regions. To faithfully compare local emissions between models we introduce a re-gridded normalization method, that also can be compared with satellite products derived from dust events frequencies. Dust total depositions are compared with instrumental network

5 to assess global and regional differences. We found that models agree with observations distant from dust sources within a factor 10, but the approximations of dust particle size distribution at emission contributed to a misrepresentation of the actual range of deposition values when instruments are close to dust emitting regions. The observational dust surface concentrations also are reproduced within a factor 10. The comparison of total aerosol optical depths with AERONETv3 stations where dust

10 is dominant shows large differences between models, however with an increase of the inter-model consistency when the simulations are conducted with nudged-winds. The increase of the model ensemble consistency also means a better agreement with observations, which we have ascertained for dust total deposition, surface concentrations and optical depths (against both AERONETv3 and MODIS-DOD retrievals). We estimated the direct radiative effects of a multi-modal representation of

15 the dust particle size distribution that includes the largest particles measured at FENNEC experiment. We introduced a method to ascertain the contributions per mode consistent with the multimodal direct radiative effects.

1 Introduction

20 Mineral dust is a key element of the Earth system. It plays an important role in our planet's energy budget, in both the long-wave (LW) and the short-wave (SW) spectrum, by direct radiative effects and feedbacks on the climate system (Knippertz and Stuut, 2014). It also contributes significantly to the global aerosol burden. Kok et al. (2017) estimated that global emissions are 1700 $\mathrm{Tg\,yr^{-1}}$ (with a range between 1000-2700 $\mathrm{Tg\,yr^{-1}}$ and particle diameters up to 20 μm) which indicates that

25 mineral dust, together with sea spray, have the largest mass emission fluxes of primary aerosols. It is transported by the atmospheric flow from emission source regions to distant remote regions up to thousands of kilometres (Kaufman et al., 2005; Li et al., 2008). When it is deposited over the ocean (Schulz et al., 2012) dust constitutes a source of minerals, in particular iron (Wang et al., 2015; Mahowald et al., 2005; Mahowald, 2011) and phosphorus (Wang Rong et al., 2014), therefore

30 it indirectly participates in the carbon cycle and the ocean removal of carbon dioxide from the atmosphere (Gruber et al., 2009; Shaffer et al., 2009). When dust is deposited over land it impacts on

Table 1. Main characteristics of the CRESCENDO models used in this study and the experiments analyzed. Resolution is given in degrees (longitude x latitude), and all dust emissions are interactively driven by wind speed. Additional information of the dust schemes can be found in the references mentioned. DPSD stands for Dust Particle Size Distribution, and supplementary information of about its modelling by each model is given in supplement material, Tables Supp.MD7 and Supp.MD8.

Model	Acronym	Resolution	Levels	Experiments	DPSD	Dust Scheme Ref.	Model Ref.
IPSL-CM6-INCA5	IPSL	2.50x1.25	79	PD, PDN, PI	modes: 1	(Schulz et al., 1998)	(Boucher et al., 2020)
CNRM-ESM2-1	CNRM-3DU	1.40x1.40	91	PD, PDN, PI	bins: 3	(Michou et al., 2020)	(Séférian et al., 2019)
CNRM-ESM2-1-CRESC	CNRM-6DU	1.40x1.40	91	PD, PDN, PI	bins: 6	(Michou et al., 2020)	(Séférian et al., 2019)
NorESM	NorESM	1.25x0.94	30	PD, PDN, PI	modes: 2	(Zender et al., 2003)	(Kirkevåg et al., 2018)
EC-Earth3-AerChem	EC-Earth	3.00x2.00	34	PD, PI	modes: 2	(Tegen et al., 2002)	van Noije et al., 2020; in preparation
UKESM	UKESM	1.87x1.25	85	PD, PI	bins: 6	(Woodward, 2001b)	(Sellar et al., 2019)
IPSL-CM6-INCA5-4DU	IPSL-4DU	2.50x1.25	79	Special PDN	modes: 4	Albani et al., 2020; in preparation	(Boucher et al., 2020)

ecosystems and snow albedo (Painter et al., 2007). In the troposphere dust contributes to heterogeneous chemical reactions (Tang et al., 2017; Dentener et al., 1996; Perlwitz et al., 2015; Bauer, 2004) and ice nucleation (Tang et al., 2016; Atkinson et al., 2013; Hoose and Möhler, 2012; Prenni et al., 2009) but also behaves as cloud condensation nuclei (Bègue et al., 2015), presenting additional in-
5   teractions with precipitation (Solomos et al., 2011). Air quality studies link dust concentrations with health effects (Monks et al., 2009) but also with visibility (Mahowald et al., 2007). Additionally, transport and deposition of dust plays a role in the design and maintenance of solar energy stations in semi-desert areas (Piedra et al., 2018), whereas at Earth's surface fine dust particles (diameter smaller than 2.5 µm can cause long-term respiratory problems (Pu and Ginoux, 2018a; Longueville
10   et al., 2010). At regional scales dust has been reported to influence the West African (Strong et al., 2015; Biasutti, 2019) and Indian monsoons (Sharma and Miller, 2017).

     As a consequence, the dust cycle is actively analysed on regional (Pérez et al., 2006; Konare et al., 2008) and global scales, based on observations and models, covering aspects related to optical properties, mineral composition, emission processes, transport and deposition (Tegen and Fung, 1994).
15 Current global models represent reasonably well the atmospheric lifetime of dust particles with a diameter of less than 20 µm (Kok et al., 2017), supporting a consistent modeling of the dust atmospheric cycle: emission, transport and deposition. Very large dust particles with diameters of several tens of micrometers are, however, seldomly represented in these models, and have become an active area of research (van der Does et al., 2018; Biagio et al., 2020).
20   Detailed comparisons between observations and models indicates that the latter are not yet capturing the full dust spatial and temporal distribution in terms of its various properties. This is due to the fact that current Earth system models are limited to approximate phenomenological descriptions of

the dust mobilization (Zender et al., 2003). These dust emissions schemes are based on either a salta­tion process (Marticorena and Bergametti, 1995) or a brittle fragmentation model (Kok, 2011), but in both cases the momentum transfer between the wind in the boundary layer and the soil particles is conditioned by erodibility or roughness surface parameters, which sometimes are simply scaled

5   to be in agreement with observations of aerosol index and/or aerosol optical depth. These constrains allow for the models to reproduce reasonably well the dust optical depth (Ridley et al., 2016) but cannot fully constrain the whole range of dust particle size distribution. This explains considerable differences in terms of surface concentrations and vertical deposition fluxes when global models are evaluated against dust observations at regional and local scales. These challenges increase in regions

10 with strong seasonal cycles and sparse vegetation cover, that require a description of the evolving vegetation, like Sahel or semi-arid regions. Others difficulties emerge when the anthropogenic com­ponent of the atmospheric dust has to be ascertained, as it requires to account for land use change and agricultural activities. Optical properties of mineral dust aerosols are another field of research as both the refractive index and the particle shape introduce uncertainties on the estimation of scatter-

15 ing and absorption properties (Nousiainen, 2009). Finally, the total mass of mineral dust emitted to the atmosphere is mostly conditioned by few events with intense surface winds, as the dust emission flux has a non-linear dependence on the wind speed, which the models pursue to capture. Actu­ally, the meteorological phenomena conditioning these events exhibit regional dependencies, e.g. in West Africa deep convection (Knippertz and Todd, 2012) and nocturnal low-level jets (Heinold

20 et al., 2013; Washington and Todd, 2005) have been found to be key drivers, while recently, (Yu et al., 2019) reported differences in the frequency of dust events between the Gobi and Taklamaklan deserts.

The relevance of dust on the Earth system implies that most climate models have introduced parametrization schemes to describe properly the dust cycle in the last two decades. Woodward

25 (2001b) describes the parametrization implemented in the Hadley Centre climate model, Miller et al. (2006) introduces the NASA Goddard dust model, Schulz et al. (1998) and later Schulz et al. (2009) show the implementation of dust emissions in the INteraction of Chemistry and Aerosols (INCA) module of the IPSL model. Pérez et al. (2011) for the BSC-DUST model, and more recently other models either incorporate new dust schemes or improved on previous ones, e.g. Albani et al. (2014)

30 and Scanza et al. (2015) in the CAM climate model, LeGrand et al. (2019) for the GOCART aerosol model, (Klingmüller et al., 2018) in the EMAC atmospheric-chemistry climate model, Colarco et al. (2014) in the NASA GEOS-5 climate model, Astitha et al. (2012) and Gläser et al. (2012) in the ECHAM climate model. Therefore comparisons to ascertain how the models are improving the description of dust related processes are needed to make progress in the above challenges. A broad

35 comparison of 15 AeroCom models (including both climate models and chemistry transport models)

Table 2. Overview of observations used for the comparison against the CRESCENDO models against observations indicating the spatial and temporal scales considered. Loadings and Mass Extinction Efficiency (MEE) were derived from models only and are compared between them. L=local, N=Network, G=Global, R=Regional, A=Annual, M=Monthly, CM=Monthly-Climatology, CA=Annual-Climatology, TS=Time-Series-Avaliable.

Diagnostic	Dataset	Spatial	Temporal	Reference	Comments
Aerosol Optical Depth	AERONET	(L, N)	(A, M, TS)	(Giles et al., 2019)	Aeronet v3
	MODIS	(G, R)	(A, M)	(Sayer et al., 2014)	DeepBlue-v6
	MISR	(G, R)	(A, M)	(Diner et al., 2002)	
Angstrom Exponent	AERONET	(L, N)	(A, M, TS)	(Giles et al., 2019)	Aeronet v3
	MISR	(G)	(A, M)	(Diner et al., 2002)	
Dust optical depth	AERONET dusty	(L, N)	(A, M, TS)	(Giles et al., 2019)	Subset of AERONET
	MODIS DOD	(G, R)	(A, M)	(Pu and Ginoux, 2018b)	See Supplementary
	IASI dust	(G, R)	(A, M)	(Peyridieu et al., 2013)	Near-Infrared
Surface concentration	UMOAC	(L, N)	(CA, CM)	(Prospero and Nees, 1986)	Filter Collectors
	Mahowald-2009	(L, N)	(CA)	(Mahowald et al., 2009)	
	INDAAF-PM10	(L)	(TS, CA)	(Marticorena et al., 2017)	INDAAF dataset
Dust deposition flux	Network-H2011	(N)	(CA)	(Huneeus et al., 2011)	Compilation dataset
	Network-SET-B	(N)	(CA)	(O'Hara et al., 2006; Vincent et al., 2016)	Compilation dataset
Wet/dry deposition flux	INDAAF-dep	(L)	(TS,CM)	(Marticorena et al., 2017)	INDAAF dataset

in terms of dust has been conducted by Huneeus et al. (2011) and more recently a comparison of 7 CMIP5 models regarding dust optical depth (Pu and Ginoux, 2018b). Albani et al. (2014) shows a detailed comparison of several dust schemes of the CAM climate model. However, as the evolution of ESMs and dust schemes continues, in parallel with the availability of longer and new/refined observations, an exhaustive comparisons of dust cycles modelling, covering scales from global to local, is still needed.

This study aims for an extensive comparison between observations and five Earth system models from Coordinated Research in Earth Systems and Climate: Experiments, kNowledge, Dissemination and Outreach (CRESCENDO) project which aims to develop the current European ESMs through targeted improvements to a range of key processes, in particular natural aerosols and trace gases. We compare the ESMs against observations in terms of optical properties (dust optical depth, Ångström exponent), surface concentration, wet and dry deposition, and dust emission, and how these aspects evolve in time and space. The paper is structured as follows: section 2 describes the models analysed, which is followed by section 3 describing the observational datasets used, and the methods (section 4). The results of the comparison are presented first at the global scale (Section 5.1), showing also its climatological spatial patterns (Section 5.2). Followed by sections describing: dust emission (Section 5.3), dust deposition (Section 5.4), dust optical depths (Section 5.5) and surface concentrations

(Section 5.6). These results are then discussed in section 6 and the main conclusion are summarised. The supplementary information is a single document but organised according with the several sections of the main paper: Supplement MD has additional information of sections 2 (models) and 3 (datasets). Supplement GL complement section 5.1. The other supplement parts refer to each of the
5   diagnostics analysed.

2   Models description

Five different Earth System Models, see table 1, constitute the CRESCENDO-ESM ensemble: CNRM-ESM2-1, NorESM1.2, EC-Earth3-AerChem, IPSL-CM6-INCA5 and UKESM. This ensemble covers the two main methods to describe the dust particle size distribution: binned/sectional and multi-
10   modal log-normal. In the sectional methodology the full size distribution is divided on a fixed number of bins while inside each bin the size distribution is considered invariant. For CNRM-ESM2-1 two different sectional descriptions based on two different bins have been evaluated, see Table S.MD.8 for further details, named here CNRM-6DU (with 6 bins) and CNRM-3DU (with 3 bins). The UKESM model includes 6 bins, with both UKESM and CNRM-6DU covering also particles
15   with diameters larger than 20µm, with two bins in the case of the UKESM model and one bin in the case of the CNRM-6DU model. In the case of modal description the evolution of the size distribution is controlled by balance equations of mass and number concentrations of each mode, as they effectively constrain a log-normal distribution with fixed width. In CRESCENDO there are two main approaches: EC-Earth and NorESM are considering bi-modal size distributions (one fine
20   or accumulation mode and one coarse mode) but mixed with other aerosols, whereas IPSL is considering a non-mixed single dust coarse mode (see Table S.MD.9). The limit between coarse and fine particles is located at about 1 µm (while accumulation refers to fine particles from 0.1 µm to 1 µm). Several experiments aimed to estimate the typical parameters of a multi-modal description of the dust size distribution: first confined to the range of sizes typical of accumulation and coarse
25   modes (Denjean et al., 2016) but also including larger particles (Ryder et al., 2018). Several studies (Adebiyi and Kok, 2020) propose that the coarse mode, and more specifically those particles with diameter larger than 20 µm are important to better understand the global dust cycle. Therefore, we also compared the CRESCENDO ESMs modal dust schemes, with a new dust scheme of the IPSL model with 4 insoluble dust modes (Albani and et al, 2020; Biagio et al., 2020) whose properties are
30   based in FENNEC campaign (Rocha-Lima et al., 2018). Table MD.9 shows the modal approaches in CRESCENDO, and how they compare with the IPSL-4DU.

   All the models provide standard approaches that estimate dust mobilization based on a velocity threshold, information on soil texture (clay/silk) and erodibility factors (including soil moisture or

accumulated precipitation). Conceptually, a fraction of the horizontal flux of dust particles, dominated by sandblasting, is actually transformed into a vertical flux with a mass efficiency factor and then effectively transported by the atmosphere. EC-Earth emissions are calculated following the scheme described by Tegen et al. (2002) based on the horizontal dust flux proposed by Marticorena

5 and Bergametti (1995), which is also used in the UKESM dust scheme (Woodward, 2001a). The NorESM emissions are estimated with the DEAD model (Zender et al., 2003). The IPSL dust emission has been described by Schulz et al. (2009, 1998), and the CNRM model (Nabat et al., 2012) used also (Marticorena and Bergametti, 1995) with an emitted size distribution based on (Kok, 2011). Although none of the models implements an explicit mineralogical description of dust particles, the

10 optical refractive index effectively accounts for global average of the mixture of minerals present in the mineral dust aerosol. Therefore those optical properties are representative for the global mineralogical composition rather than a description of the soil-type dependence of the mineralogy that would imply local differences on emitted optical properties. This approximation is considered to drive specific bias on those regions with the fraction of hematite or goethite minerals induce larger

15 values of optical absorption.

In all the models the particle size is described by the geometric diameter, where the dust particles with irregular shapes are modelled by spherical particles with the same effective volume. Regarding optical properties they are calculated based on Mie scattering, this approximation is reasonable as far as the orientation of the particles is randomly distributed, but any physical process that breaks

20 this hypothesis, like preferential transport of specific geometries or physical processes that promote a specific orientation of the particles, will imply bias in the methodology. Additionally, the spherical approximation is considered to underestimate the optical extinction of mineral dust (Kok et al., 2017). This hypothesis also affects the actual area of the global mineral dust surface which is important in heterogeneous chemistry (Bauer, 2004) and influences tropospheric chemistry. The geometry

25 of the particles also affects the gravitational settling, and therefore the transport of particles with specific geometries (Li and Osada, 2007) and their lifetime in the atmosphere.

2.1 Model experiments

Because the models have interactive dust emissions, wind fields play a prominent role on dust emission and transport (Timmreck and Schulz, 2004). Therefore, this study contrasts two differ-

30 ent present-day forcing experiments: one with winds generated by the dynamical part of the climate model (named PD), and the other nudged to re-analysed winds from ERA-Interim (named PDN). The historical greenhouse gases concentrations are consistent with (Meinshausen et al., 2017). The models IPSL and IPSL-4DU without explicit gas-phase interactive chemistry activated use the CMIP6 ozone forcing database (Checa-Garcia et al., 2018; Checa-Garcia, 2018). The CNRM-ESM2-1 has
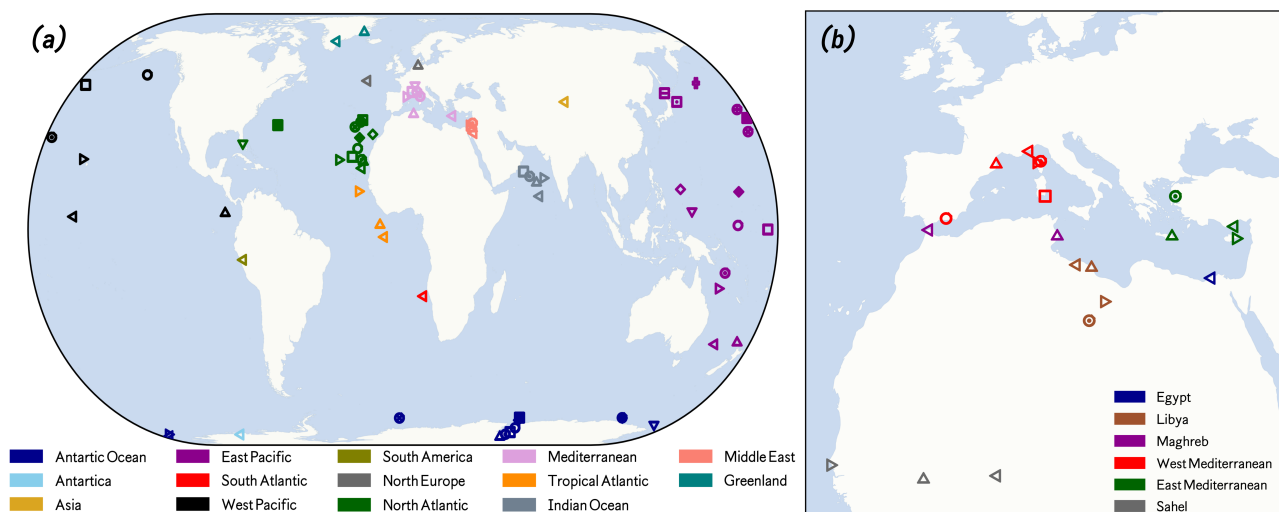
Figure 1. Panel (a): Stations of the dataset named H2011 which collects annual dust deposition fluxes for multiple years (Huneeus et al., 2011). Panel (b): Dataset named SET-M which collects additional stations in the Mediterranean region were observations have been reported by (O'Hara et al., 2006; Vincent et al., 2016), and stations over Sahel (Marticorena et al., 2017). The different colors represent the region where each station belongs to.

explicit chemistry at the stratosphere and upper-atmosphere (Michou et al., 2020). A last simulation where aerosols and chemistry emissions are prescribed for 1850 (named PI) is presented as well, see Table 1. All the simulations are from 2000 to 2014 plus at least 1 year of spin-up (except NorESM-PDN that covers 2001 to 2014). All the simulations implement prescribed SSTs of present-

5 day conditions. The additional CRESCENDO simulation named PI-PIsst with pre-industrial SST is not analysed in this study.

3 Observational datasets

The observational datasets used to ascertain the performance of the CRESCENDO ESMs in their representation of mineral dust are based on a compilation of ground-site and satellite measurements.

10 Table 2 summarizes the different available datasets used, and the spatial and temporal scales applied in the analysis. Additionally, this table includes datasets representative of either a monthly or a yearly climatology (respectively referred as CM and CA in Table 2). In this section these datasets are briefly described but we refer to original publications for further details. For those datasets with specific pre-processing the additional details are given in the supplementary material.

3.1 Surface Deposition flux

This dataset comprises the deposition flux observations described in Huneeus et al. (2011), composed from several measurements campaigns over land and ocean (Figure 1 panel a), and named hereafter *Network-H2011*, plus an additional set of measurements at stations in the Mediterranean and Sahel

5 regions (Figure 1 panel b), named hereafter *Network-SET-M* for which data values are shown on Table S.MD.5.

The set *Network-H2011* gives deposition fluxes estimated from sedimentation corresponding to DIRTMAP database (Kohfeld and Harrison, 2001), while direct measurements of deposition fluxes were acquired during the SEAREX campaign (Ginoux et al., 2001) mostly in the Northern Hemi-

10 sphere. Mahowald et al. (2009) describes 28 sites where dust deposition is inferred assuming a 3.5% fraction of iron. The compilation also includes observations of deposition fluxes deduced from ice core data according to Huneeus et al. (2011). The dataset covers a range of total dust flux depositions from 10^{-3} to $0.5 \cdot 10^3 \, \mathrm{g \, m^{-3} yr^{-1}}$ but without a homogeneous distribution of values over this range. Only two stations have observational values larger than $100 \, \mathrm{g \, m^{-2} yr^{-1}}$ and the bulk set of stations

15 comprised values between 0.1 and 75 $\mathrm{g \, m^{-2} yr^{-1}}$.

The dataset *Network-SET-M* includes field measurements for 20 additional stations located in the Mediterranean and Sahel regions to represent both deposition near to dust sources (O'Hara et al., 2006), as well as at intermediate distances from them (Vincent et al., 2016). The values in this dataset ranges values from 4.2 to 270 $\mathrm{g \, m^{-2} yr^{-1}}$ and allow us to visualize regional differences in

20 dust deposition flux. The INDAAF stations (Marticorena et al., 2017) provide us with an estimation of the inter-annual variability which is large on Sahel region (see the Table S.MD.7)

3.2 Surface concentrations

A first part of the climatological dataset for dust concentrations (see Table S.MD.4) at the surface has been adopted from estimations done by the University of Miami Oceanic Aerosols Network

25 (UMOAN) whose instruments are filter collectors deployed in the North Atlantic and Pacific Oceans (Prospero and Nees, 1986; Prospero and Savoie, 1989). This dataset provides climatological monthly averages with a standard deviation that represents inter-annual variability. The second part of the climatological dataset is based on yearly values from the stations data shown in (Mahowald et al., 2009). The dataset comprises 36 stations with values from $5 \cdot 10^{-2}$ to $100 \, \mu \mathrm{g \, m^{-3}}$ distributed within

30 the full range of values but grouped in clusters correlated with the geographical regions they belong to.
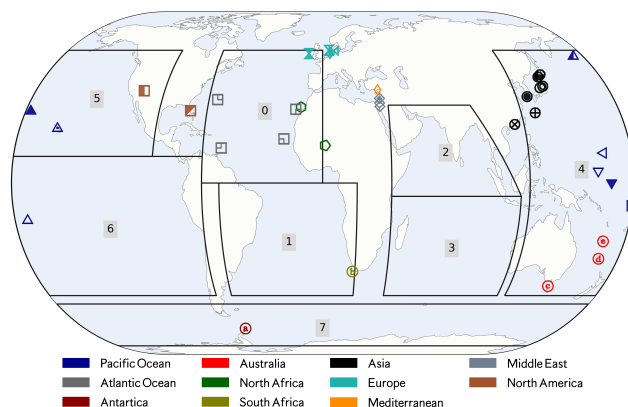
Figure 2. Maps with 36 stations where surface concentration was monitored by UMOAC (University of Miami Oceanic Aerosols Network) and also those described by Mahowald et al. (2009). Colors represent the region where each station belongs to. The regions correspond to those used for the regional analysis of dust deposition over the ocean: North Atlantic (0), South Atlantic (1), North-Indian Ocean (2), South-Indian Ocean (3), Pacific East (4), Pacific North-West (5), Pacific South-West (6) and Antarctic Ocean (7).
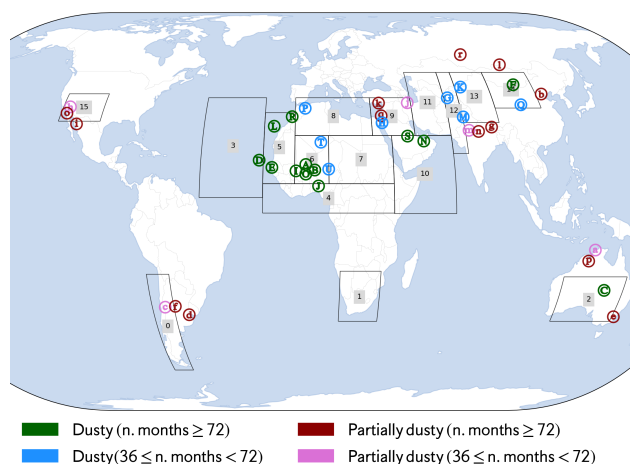
Figure 3. Maps of 39 dusty stations from AERONET, classified in two groups: 21 dust-dominated stations (uppercase letters), and 18 stations where dust is important but not necessarily dominant (lower-case letters). The colors allows to differentiate also the number of months in the observed time-series. The regions for the preferential dust emission sources (plus Mid-Atlantic region) are indicated with numbered boxes. The region number correspond to the names of the regions to which they belong: South-America (0), South-Africa (1), Australia (2), Mid-Atlantic (3), Sahel/Gulf of Guinea (4), Western Sahara (5), Mali/Niger (6), Bodele/Sudan (7), North Sahara (8), North MiddleEast (9), South-MiddleEast (10), Kyzyl Kum (11), Thar (12), Taklamakan (13), Gobi Desert (14), North-America (15).

Table 3. Given the mass mixing rations X_s, airmass a_{mass}, optical depths τ_s per specie s and air density ρ_{air}. We indicate here the method used to estimate other diagnostics. (i,j) are the coordinates/index of each cell grid, l represent the level/layer. $A(i,j)$ is the area of (i,j) grid cell, l_0 represent the surface layer

Diagnostic	Symbol	Equation	Units
Grid cell area	$A(i,j)$	Diagnostic provided by models	kg
Mass mixing ratio	$X_s(i,j,l)$	Diagnostic provided by models	$\mathrm{kg\,kg^{-1}}$
Air-mass	$a_{mass}(i,j,l)$	Diagnostic provided by models	kg
Optical depth at 550nm	$\tau_s(i,j)$	Diagnostic provided by models	-
Grid cell loadings	$L_s(i,j)$	$\sum_l \left[X_s(i,j,l) \cdot a_{mass}(i,j,l) A(i,j)^{-1} \right]$	$\mathrm{kg\,m^{-2}}$
Total loading	TL_s	$\sum_{i,j} L_s(i,j) A(i,j) = \sum_{i,j,l} X_s(i,j,l) \cdot a_{mass}(i,j,l)$	kg
Surface concentrations	$\widetilde{x_s}(i,j)$	$X_s(i,j,l_0) \cdot \rho_{air}(i,j,l_0)$	$\mathrm{kg\,m^{-3}}$
Mass Extinction Efficiency at 550nm	$m_s^{ee}(i,j)$	$\tau_s(i,j) L_s(i,j)^{-1}$	$\mathrm{kg^{-1}\,m^2}$

3.3 INDAAF stations of data

The multi-instrument network was deployed in the frame of the African Monsoon Multidisciplinary Analysis, and belongs to the INDAAF set of data-stations. Marticorena et al. (2010) described the collocated measurements of wet and dry deposition, as well as, surface concentrations (of particulate matter smaller than 10 µm) at three stations in the Sahel region, see Tables S.MD.6 and S.MD.7 and Figure 1 panel (b). The stations also measured precipitation, wind velocity and surface temperature. Additionally, in the same location there are AERONET sun-photometers to measure aerosol optical depths.

3.4 AERONET optical properties

The AERONET database implemented in our comparisons rely on the Version 3 (Level 2.0) algorithm. Based on this new algorithm the entire database of observations has been reprocessed in 2018 (Giles et al., 2019). The database comprises aerosol optical depths and Ångström exponents, as well as, fine and coarse optical properties obtained with a new cloud-screening quality control scheme. The actual division threshold between fine and coarse particles is ascertained by the inversion algorithm that aims to differentiate aerosol particles from ice crystals and it lies between 0.44 and 0.99 µm

The network database provides daily data, allowing for events analysis, and there is also a monthly time resolution dataset, used here to examine decadal, yearly and seasonal properties. We processed the 300 stations from the full network to explore general properties and we selected those stations where it is considered that mineral dust is an important part of the aerosol composition based on the

Table 4. Statistics used to compare with observations and perform model inter-comparisons. N indicates the number of observations or sample size. When the analysis refers to a global performance of the model over a set of instruments, N represents the number of stations. When the statistical analysis is done over a time series of values, N represents the number of time samples usually corresponding to an specific location. Pearson Correlation Coefficient (ρ), bias (δ), normalized bias (δ_N), Ratio standard deviations (Σ), Normalized mean absolute error (θ_N) and Root mean square error (RMSE=η).

Statistic Estimator
$\rho = Cov(log_{10}X, log_{10}Y)/(\sigma(log_{10}X)\sigma(log_{10}X))$
$\delta = N^{-1}\sum_{i=1}^{N}(x_i^{(mod)} - x_i^{(obs)})$
$\delta_N = \sum_{i=1}^{N}(x_i^{(mod)} - x_i^{(obs)})/(\sum_{i=1}^{N} x_i^{(obs)})$
$\Sigma = \sigma_{mod}/\sigma_{obs}$
$\theta_N = \sum_{i=1}^{N}\left|x_i^{(mod)} - x_i^{(obs)}\right|/(\sum_{i=1}^{N} x_i^{(obs)})$
$\eta = N^{-1}\sqrt{\sum_{i=1}^{N}(x_i^{(mod)} - x_i^{(obs)})^2} = RMSE$

presence of dust at the geographical position by all the models. This subset is named here dusty set of stations, which are shown in Figure 3. It comprises 39 stations divided on two subsets: those stations where the dust has a *dominant* role in terms of optical depths ($\tau_{440}^{dust} > 0.5\tau_{440}^{all-aer}$ for all models along the seasonal cycle), and those where the dust is *important* although not necessary dominant for

5 all the models (even if for a specific model but not all the dust optical depth contributes with more than 50% of the total aerosol optical depth). The first subset comprises 21 stations and it is noted with upper-case letters in Figure 3. The second has 19 stations, noted with lower-case letters. The dusty stations set over Africa is consistent with the stations analysed by Huneeus et al. (2011) based on Bellouin et al. (2005) criteria, but it has been extended with stations Australia, South-America,

10 North-America and Asia consitent on (Klingmüller et al., 2018). Figures with the seasonal cycle of aerosol optical depths of the dusty dominant and important stations seasonal cycle that highlight the classification criteria are shown in the supplement material (Figures S.DOD.10 and S.DOD.11).

3.5 MODIS dust related products

Interactions between dust and radiation are defined through three optical properties: dust optical

15 depth (DOD), single scattering albedo (ω) and the asymmetry parameter which defines the ratio of the radiation scattered forward over the scattered backward. For the dust coarse mode, the dust optical depth can be estimated using the Moderate Resolution Imaging Spectro-radiometer (MODIS) enhanced deep-blue (DB) aerosol optical depth (Sayer et al., 2014) as done by Pu and Ginoux (2018b) with the additional support of the MODIS product of single-scattering albedo (ω) and Ångström

Table 5. Global dust mass balance, dust loading, dust optical depth (DOD), mass extinction efficiency (MEE) and lifetime for each model and each experiment available. CNRM has two configurations one specific for CRESCENDO noted as CNRM-6DU and another for CMIP6 noted as CNRM-3DU. The UKESM is not providing the dust sedimentation so dry deposition include all not wet deposition fluxes for this model. The units for emissions and depositions tendencies are Tg yr^{-1}, for Load is Tg, for MEE is $m^2 g^{-1}$ and lifetime in days. MEE is calculated as the mean of the MEE(x,y) field, while $\widehat{MEE}$ is the ratio of DOD and Load mean fields. Δ represents the ratio of the Net (Emission-Total Deposition) relative to emission in %. $\mathcal{R}_{dep}$ is the ratio of total dry (including gravitational settling) over total wet deposition. MM-mean shows the multi-model mean for each experiment and MM-σ the estimated multi-model standard deviation. Note that some statistical estimations (indicated with $\ddagger$) related to the deposition are not including the UKESM model as we can't know separate the gravitational settling from other dry deposition processes.

Model	Exp.	Emi. [Tg yr^{-1}]	Dep. [Tg yr^{-1}]	Net [Tg yr^{-1}]	Δ %	Dry Dep. [Tg yr^{-1}]	Wet Dep. [Tg yr^{-1}]	Sedim. [Tg yr^{-1}]	$\mathcal{R}_{dep}$	DOD -	Load [Tg]	$\widehat{MEE}$ [$m^2 g^{-1}$]	MEE [$m^2 g^{-1}$]	Lifetime [day]
CNRM-6DU	PD	3542.2	3392.8	149.41	4.24	542	2108.9	741.9	0.61	0.023	32.6	0.55	0.36	3.4
CNRM-3DU	PD	2605.2	2461.9	143.29	5.5	1490.3	753.8	217.8	2.27	0.011	13.3	0.63	0.44	1.9
EC-Earth	PD	1126.6	1126.7	-0.12	-0.01	367.8	493.2	265.7	1.28	0.029	11.7	1.86	1.27	3.8
IPSL	PD	1557.5	1558.9	-1.44	-0.1	329.3	968.3	261.3	0.61	0.026	16.4	0.82	0.82	3.8
NorESM	PD	1368.2	1368.3	-0.09	-0.01	84.0	275.7	1008.6	3.96	0.023	7.2	2.86	1.63	1.9
UKESM	PD	7524.4	7527.6	-3.21	-0.04	6566.3†	949.8	-	6.91	0.011	18.1	0.5	0.31	0.9
MM-mean	PD	2954.0	2906.0			562.7‡	920.0‡	499.0‡		0.020	16.5	1.20	0.80	2.6
MM-σ	PD	2415.0	2414.0			543.7‡	714.3‡	356.6‡		0.008	8.7	0.95	0.54	1.2
CNRM-6DU	PI	3887.3	3734.3	153.06	3.96	597.4	2319.1	817.7	0.61	0.012	35.2	3.2	0.17	3.3
CNRM-3DU	PI	2651.5	2509.8	141.76	5.34	1508.3	781.0	220.4	2.21	0.012	13.4	0.63	0.44	1.8
EC-Earth	PI	1145.8	1145.4	0.44	0.04	374.4	511.6	259.4	1.24	0.027	11.6	1.7	1.17	3.7
IPSL	PI	1551.7	1553.2	-1.49	-0.1	330.6	961.0	261.5	0.62	0.027	16.7	0.82	0.82	3.9
NorESM	PI	1407.3	1407.5	-0.21	-0.01	86.8	287.4	1033.2	3.90	0.023	7.4	2.75	1.56	1.9
UKESM	PI	7421.9	7413.6	8.25	0.11	6475.6†	938.0	-	6.90	0.01	17.4	0.49	0.29	0.9
MM-mean	PI	3010.9	2960.1			579.5‡	972.0‡	518.4‡		0.018	16.9	1.20	0.74	2.58
MM-σ	PI	2388.9	2378.9			549.9‡	795.6‡	379.6‡		0.008	9.7	0.95	0.54	1.21
CNRM-6DU	PDN	1278.4	1216.3	62.09	4.85	208.6	716.8	290.9	0.70	0.011	15.2	0.56	0.38	4.3
CNRM-3DU	PDN	1812.1	1725.7	86.41	4.77	1126.5	435.1	164.0	2.97	0.011	11.6	0.63	0.46	2.3
IPSL	PDN	1295.3	1297.1	-1.77	-0.13	268.8	813.1	215.2	0.60	0.024	14.8	0.82	0.82	4.2
NorESM	PDN	1733.6	1733.4	0.12	0.01	115.7	345.5	1272.2	4.02	0.029	9.1	2.87	1.61	1.9
MM-mean	PDN	1529.9	1493.1			429.9	577.6	485.6	2.07	0.019	12.7	1.22	0.82	3.18
MM-σ	PDN	282.5	275.0			468.7	222.9	527.0	1.70	0.009	2.9	1.11	0.56	1.25

† Values including the sedimentation. ‡ Statistic is not including UKESM.

exponent (α). The rationale of the method relies on the properties of these three optical parameters applied to aerosols particles. First, α is very sensitive to particle size, so there are parametrizations of aerosol optical depths that use it to separate each mode contribution. Second, aerosols with low absorption and large scattering like sea-salt have $\omega \simeq 1$, whereas mineral dust is considered an ab-

5 sorbing aerosol. Third, the dependency of $\alpha(\lambda)$ in wavelength contains a signature of the aerosol composition. Given this information, we have considered 2 different MODIS dust optical depth related datasets. One of them is a pure filter of aerosol optical depth to differentiate those pixels where dust is expected to be the dominant contribution to aerosol optical depth, but without the attempt to estimate the actual fraction of mineral dust, so it is considered here as an upper threshold of the

10 actual DOD of the coarse mode (because particles of dust with diameters below 1 µm are thought to contribute less and 10% to total dust optical depth). The other method aims to explicitly separate sea-salt, and proceed to re-scale the aerosol optical depth to ascertain an actual value of DOD, according to Pu and Ginoux (2018b) it may be considered a lower-bound of the DOD. Additional information and a comparison of these created products are given in the supplementary information,

15 see Figures S.MD.2 and S.MD.3.

3.6 MISR aerosol optical depth derived products

The Multi-angle Imaging Spectro-Radiometer (MISR) is a sensor on-board the Terra satellite which takes advantage of its multi-angle measurements capabilities. It is able to ascertain the presence of non-spherical particles on the aerosol products at four different wavelengths. The optical depth at

20 several wavelengths has been used to compute the Ångström exponent between Mar-2000 and Dec-2014 of MISR, and compare with the models Ångström exponent based in the same information. This product gives us information on how the models represent the spectral dependence of optical depth. Our computation using the 446 nm and the 672 nm wavelength, has been compared with MISR Ångström exponent product to validate our computations, see Figure S.GL.8.

25 4 Methods

Along this study we calculated several diagnostics not directly provided by the different models. Table 3 shows how they has been estimated together with the units used. Regarding the statistical methods, Table 4 shows the statistics definitions used for the comparison of models with network of instruments. The skill of the models to ascertain the dust optical depth over dust source regions

30 has been calculated based on the Pearson correlation. Given that this statistics is not robust and it is unable to inform about non-linear relationships, the skill is also estimated based on the Spearman rank correlation.
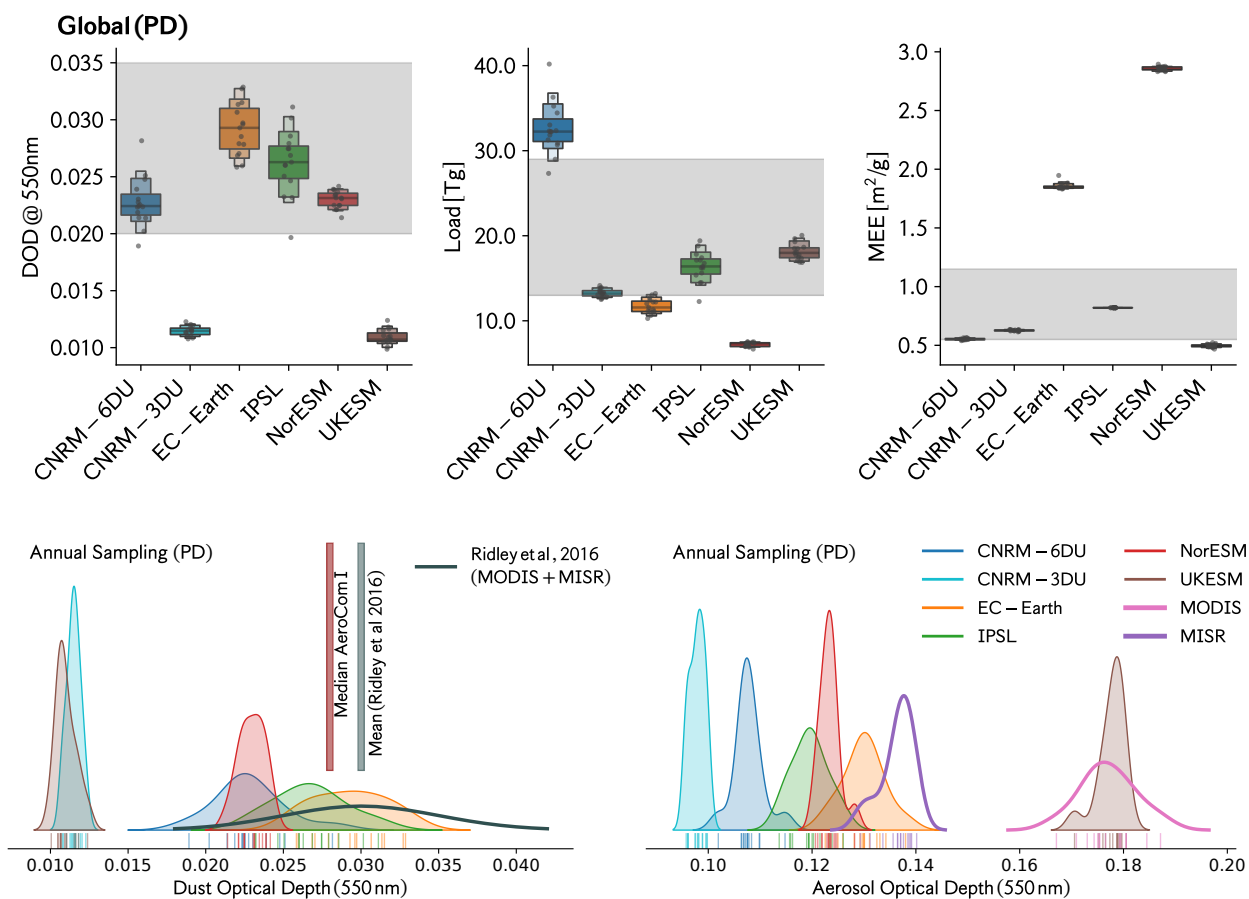
Figure 4. Top panel: Global dust cycle values for PD experiment. The gray shaded region represents the expected interval based on (Kok et al., 2017) for dust particles with diameter up to 20 μm for Dust Optical Depth, Loadings and mass extinction efficiency (MEE). Bottom left panel represents the estimated distribution of global dust optical depth annual values (samples are the marks on x-axis). The bottom right panel is the analogous for all aerosols optical depth. Both distributions are normalized and vertical axis represents a probability. Additional analysis analogous to top panel but constrained over different regions are in supplement material (figures S.GL.1 and S.GL.2).

For the comparison against the networks of instrument used: one monitoring surface concentrations, two for total deposition and one that retrieves dust optical depths, we proceed with the same methodology. For each observation, we chose the model value of the corresponding variable in the grid pixel to which this measuring station belongs. Given the different area covered by the grid

5   cell and the pointed location of the in-situ measurement, there is an underlying representation error. However, the observational datasets of total deposition and surface concentrations at point based sites are climatological estimations which can be representative of larger areas. The values for the parameters discussed here are time averaged over the 15-year simulations and hence the produced fields are smooth over subgrid scales.

10   Table 4 summarizes the statistical metrics used to evidence differences between models and observations. The surface concentration and total deposition comparison are presented as scatter-plots together with three associated statistics: the Pearson correlation (evaluated in log-scale), the bias and the RMSE. These last two metrics can be used to characterize quantitative differences between each model and observations. Tables 10, 11 and 12 include in addition, the normalized bias and the

15   normalized mean absolute error which help us understand how the models differ when scaled to the observation values.

5   Results

The results are divided in six different subsections. First a comparison at the global scale summarises the main properties of the global dust cycle in the models analyzed, which is complemented with an

20   overview of the spatial pattern of the temporal mean of the 15 years of simulation (based on monthly values) for each of the climate models of the study. The next four sections are detailed analysis of the dust properties: emission, deposition, optical depth and surface concentrations. Each one is described at regional scale and compared against network of instruments and/or satellite retrievals when available. In all the cases, the PD experiment simulations has been taken as the baseline of the

25   inter-comparison and shown in the main paper. The results for other experiments (PDN and PI), if not present in the main paper, are shown in the supplementary material. The case of nudged wind simulations (PDN) is used to ascertain the role of modelled surface winds on inter-model differences, whereas the other based on PI simulations help us to evaluate a possible role of prescribed emissions.

5.1   Global dust properties

30   The global dust cycle have been analysed in terms of global climatological values and complemented by an study of the role of the particle size distribution on the direct radiative effects (based in the IPSL model with 4 dust modes).

Table 6. Direct Radiative Effects (DRE) at the top of the atmosphere and surface without clouds for long-wave and short-wave. IPSL model with 4 dust modes as described by (Albani and et al, 2020). For each mode it is indicated the value with each method (*in* and *out*) and their mean value (in italic). Both methods are described in the appendix A. Values in italic represent those derived by other values of the table. The mean value of the sum of the 4 modes is consistent with the value of the multi-modal DRE of dust.

Dust DRE	TOA LW [W m^{-2}]			TOA SW [W m^{-2}]		
	in	*out*	*Mean*	*in*	*out*	*Mean*
Mode m_1	0.0074	0.0063	*0.0069*	-0.1360	-0.0932	*-0.1146*
Mode $m_{2.5}$	0.0399	0.0349	*0.0375*	-0.2737	-0.2300	*-0.2518*
Mode m_7	0.0913	0.0848	*0.0881*	-0.0779	-0.0440	*-0.0609*
Mode m_{22}	0.0110	0.0087	*0.0099*	0.0188	0.0139	*0.0163*
$\sum$ modes	*0.1497*	*0.1348*	*0.1422*	*-0.4689*	*-0.3533*	*-0.41*
Multimodal			0.142			-0.41

Dust DRE	SRF LW [W m^{-2}]			SRF SW [W m^{-2}]		
	in	*out*	*Mean*	*in*	*out*	*Mean*
Mode m_1	0.0194	0.0142	*0.0168*	-0.2367	-0.1854	*-0.2110*
Mode $m_{2.5}$	0.1180	0.0910	*0.1045*	-0.6413	-0.5378	*-0.5895*
Mode m_7	0.3217	0.2831	*0.3024*	-0.6615	-0.5548	*-0.6082*
Mode m_{22}	0.0540	0.0371	*0.0455*	-0.0653	-0.0442	*-0.0547*
$\sum$ modes	*0.5131*	*0.4253*	*0.4692*	*-1.6047*	*-1.3223*	*-1.4635*
Multimodal			0.467			-1.45

The dust particle size distribution is physically constrained by emission, transport and deposition (wet and dry), whereas, other aerosol processes like aerosol nucleation, condensation and coagulation have a minor role on the evolution of this size distribution (Mahowald et al., 2014). Therefore, the first step to describe the global atmospheric dust cycle in climate models consists of a charac-
5   terization of the emission and deposition fluxes at surface. This analysis is complemented by the analysis of two size-integrated properties: the dust optical depths and loadings. Other phenomena present in the Earth System dust cycle on long timescale derived from the stabilization of dust deposition over surface on long time-scales are not considered in this work as they are relevant for paleoclimate studies of dust cycle.
10   The global dust budget is analysed for the whole period of the simulations over the three different simulations considered: PD, PDN and PI. Table 5 presents the mean global values of each model. It describes the dust mass balance in terms of emission, dry and wet deposition, and the parameter
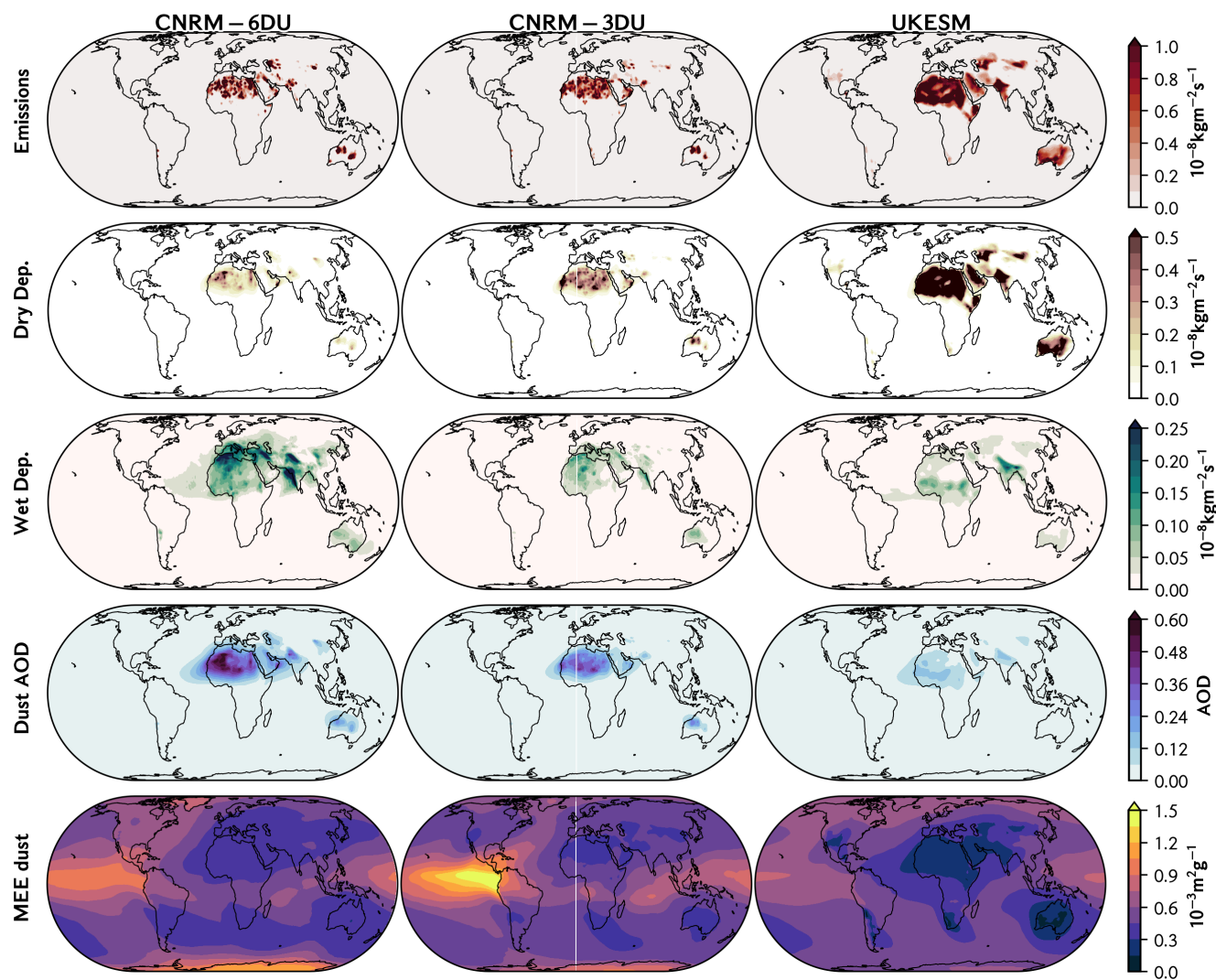
Figure 5. CRESCENDO-ESMs global maps describing dust properties (averaged over the 15 years): emission tendency, depositions tendencies, dust optical depths and mass extinction efficiency. The models included have a bin-based dust parametrization, these models are: CNRM-6DU, CNRM-3DU and UKESM models. The equivalent figures for PI and PDN experiments are shown in supplement material: figure S.GL.3 and figure S.GL.4 respectively.

Δ ascertains the fraction (%) of the emissions not deposited relative to the total emission. $\mathcal{R}_{dep}$ represents the ratio of total dry to total wet deposition.

For global emissions, the PD and PI experiments the multi-model mean 2954 Tg yr^{-1} and 3011 Tg yr^{-1} respectively. The PDN experiment shows an ensemble mean value of 1530 Tg yr^{-1} which is

significantly smaller as UKESM is not present but also because an important decrease on the CNRM-3DU and CNRM-6DU total emissions. This value agrees well with recent estimations (Kok et al., 2017) when large particles (diameter ≤ 20 µm) are not included, and previous estimations of 1500 $\mathrm{Tg\,yr^{-1}}$ based on the DEAD model (Zender et al., 2003) for particles with D<10µm. Also when

5 nudged winds are used (PDN ensemble), the standard deviation of total emissions (282 Tg yr^{-1}) is significantly smaller than in PD or PI cases. For the PD experiment the multimodel ensemble total emission for the same models that those of PDN experiment has a mean value of 2268 $\mathrm{Tg\,yr^{-1}}$ with a standard deviation of 1000 $\mathrm{Tg\,yr^{-1}}$.

The CNRM-6DU and CNRM-3DU models have total emissions with nudged winds similar to

10 the CRESCENDO-ESMs ensemble mean, but they produce higher emissions without nudged wind-field, i.e. 2600 $\mathrm{Tg\,yr^{-1}}$ in CNRM-3DU model (diameters up to 10 µm), and 3500 $\mathrm{Tg\,yr^{-1}}$ for CNRM-6DU (diameters up to 50 µm, see Table 1). These values are similar to the 3000 $\mathrm{Tg\,yr^{-1}}$ reported by Tegen and Fung (1994) for particle sizes between 0.1 and 50 µm. Due to the presence of particles with diameters up to 62 µm, the UKESM model has notably higher emissions (although in

15 this case we can't assess the role of surface winds). These large particles sediment faster as shown by the monthly mean global loadings with values close to the other models, and the smaller lifetime of dust in the atmosphere (less than 12 hours, a characteristic value of larger particles).

The mass budget of CNRM-6DU and CNRM-3DU models are only closed within $\Delta \simeq 4.5\%$ as their dynamical cores are based on a semi-Lagrangian method (Voldoire et al., 2012, 2019) which

20 is not fully mass conservative in terms of the tracers. The deposition value therefore represents a lower threshold to actual values since a fraction of the emitted mass is effectively deposited (during long-term transport) but not accounted for in deposition fluxes. For the other models $\Delta < 0.1\%$, with NorESM and EC-Earth presenting values closest to zero. Regarding the deposition of larger particles for UKESM the dry deposition (which for this model includes sedimentation) is truly dominant,

25 resulting in a wet deposition close to other models without the largest particles modelled like IPSL. In CNRM-6DU wet deposition is two times larger than those of UKESM or IPSL models at PD simulation (being the only model for which wet deposition exceed total dry deposition) but close to IPSL with nudged winds. Because larger particles are deposited faster by gravitational settling, it is expected that $\mathcal{R}_{dep}$ would be larger for those models including the largest particles, but it is only

30 obvious for the UKESM model. For CNRM-6DU model that is not the case. EC-Earth doubled the value of $\mathcal{R}_{dep}$ of IPSL, and NorESM is 6 times larger. Previously, Shao et al. (2011) reported values for $\mathcal{R}_{dep}$ between 1.03 and 8.1 also uncorrelated with the size range of the dust particle modelled. The multimodel ensemble mean for total dry deposition is 562.7 $\mathrm{Tg\,yr^{-1}}$ for PD experiment and 430 $\mathrm{Tg\,yr^{-1}}$ for PDN, in the case of wet deposition we estimated 920 and 577 $\mathrm{Tg\,yr^{-1}}$ multimodel

35 mean for PD and PDN experiments respectively.
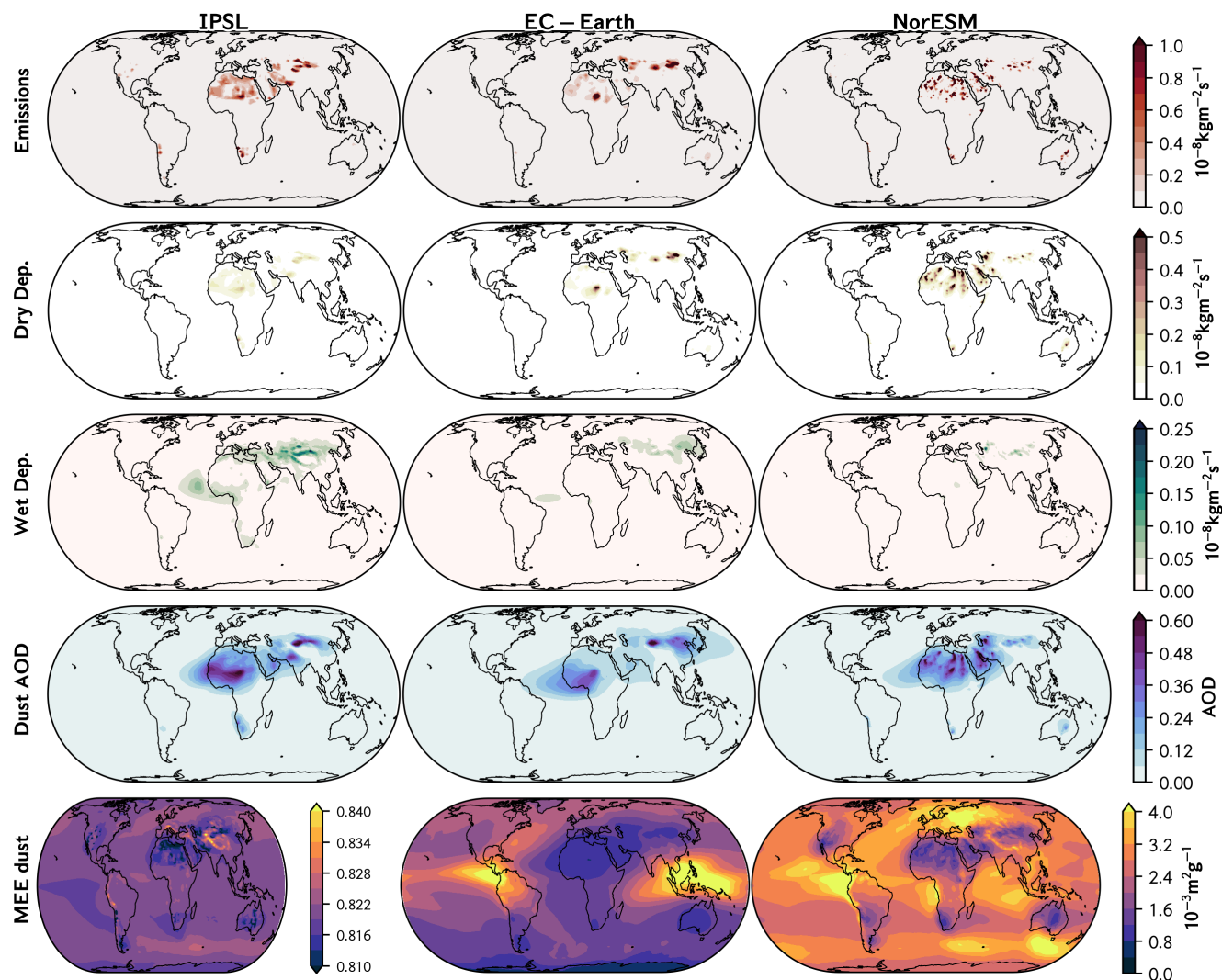
Figure 6. CRESCENDO-ESMs global maps of dust properties (averaged over the 15 years): emission tendency, depositions tendency, dust optical depths and mass extinction efficiency. The models included have a modal based dust parametrisation, these models are: IPSL-INCA, NorESM and EC-Earth. The equivalent figures for PI and PDN experiments are shown in supplement material: figure S.GL.5 and figure S.GL.6 respectively.

Atmospheric Chemistry and Physics Discussions — Open Access

Table 7. First part of the table: Emissions [Tg yr^{-1}] for Present Day (PD). Globally, over Land and over coastline pixels. (*) Denotes those models with bin sizes larger than 10 μm. Sahara desert emissions and its percentage over total emissions is obtained from the sum of the regions: Western Sahara, Mali, Bodele and North Sahara, so it is not including Sahel. Second part of the table: Emissions [Tg yr^{-1}] for Present Day (PD) simulations. Over 16 different regions, see Figure 3. In brackets the order of the 10 regions with largest emissions. The multimodel ensemble the table includes the mean values ± the standard deviation for all the models, and for all the models without UKESM. On the supplement material (section E), the tables E1 to E4 have the analogous information for PI and PDN experiments.

	CNRM-6DU (PD)		CNRM-3DU (PD)		EC-Earth (PD)		IPSL (PD)		NorESM (PD)		UKESM (PD)		MM-mean (PD)		‡MM-mean (PD)	
Global Earth	3542.2	(*)	2605.2	(*)	1126.6		1557.5		1368.2		7524.4	(*)	2954	(± 2415)	2040	(± 1012)
Land	3377.4	(*)	2526.1	(*)	1111.0		1550.9		1343.6		7506.4	(*)	2903	(± 2410)	1982	(± 948)
Ocean (Coast)	164.8	(*)	79.1	(*)	15.6		6.6		24.6		18	(*)	52	(± 61)	58	(± 66.)
Sahara Desert	2071.5	(58%)	1734.2	(66%)	445.2	(39%)	715.4	(46%)	651.8	(48%)	4339.5	(58%)	1660	(± 1466)	1124	(± 728)
North. Hemis.	3135.3	(88%)	2292.7	(88%)	1072.9	(95%)	1377.6	(88%)	1256.1	(92%)	6614.9	(89%)	2625	(± 2104)	1827	(± 870)
South. Hemis.	406.9	(12%)	312.5	(12%)	53.7	(5%)	179.9	(12%)	112.1	(8%)	909.5	(11%)	329	(± 313)	213	(± 145)
South America	17.4		13.3		11.3		36.9		9.0		18.2		18	(± 10)	18	(± 11)
South-Africa	5.8		17.0		2.8		113.8	(5)	31.8		30.3		34	(± 41)	34	(± 46)
Australia	343	(4)	235.4	(5)	35.9	(9)	10.7		59.3	(4)	691.2	(5)	229	(± 261)	137	(± 145)
Western Sahara	242.5	(6)	296.1	(4)	52.1	(6)	87.4	(6)	95.8	(6)	788.8	(4)	260	(± 276)	155	(± 108)
Mali/Niger	382.4	(3)	323.2	(3)	49.5	(7)	83.4	(8)	69.5	(3)	841.2	(3)	292	(± 304)	182	(± 158)
Bodele/Sudan	540.4	(2)	569.4	(1)	259.6	(2)	305.8	(1)	190.6	(2)	1852.2	(1)	620	(± 623)	373	(± 171)
North Sahara	906.2	(1)	545.5	(2)	85.0	(4)	238.8	(2)	295.9	(1)	857.3	(2)	488	(± 339)	414	(± 321)
North-MiddleEast	253.7	(5)	112.8	(9)	17.0		28.1		146.1	(5)	303.7	(8)	144	(± 117)	112	(± 97)
South-MiddleEast	208.0	(8)	195.9	(6)	39.5	(8)	68.1	(9)	83.7	(8)	441.1	(6)	173	(± 149)	119	(± 77)
Kyzyl Kum	230.3	(7)	118.7	(7)	118.8	(3)	142.4	(4)	198.7	(7)	377.4	(7)	198	(± 99)	162	(± 50)
Thar	136.3		56.1	(9)	19.1		86.2	(7)	13.9		288.7	(9)	100	(± 103)	62	(± 51)
Taklamakan	15.2		15.7		104.6	(4)	153.0	(3)	35.5		75.0		67	(± 55)	65	(± 61)
Gobi	140.2	(9)	36.2		269.8	(1)	113.1	(6)	80.6	(9)	230.3		145	(± 89)	128	(± 88)
North-America	0		1.1		2.3		28.4		6.1		57.1		15.8	(± 23)	7.6	(± 12)

‡ These statistics are not including UKESM.

The impact of the largest particles on global behaviour of dust optical depth and loadings is considered less important than coarse particles (up to 10 μm), so this allows us to compare with observational constrains that rely on optical depth measurements. Figure 4 (top panel) compares the PD experiment with the Kok et al. (2017) proposed values of dust optical depth and total load, whereas

5   in addition we derived the mass extinction efficiency (MEE) field as the ratio of dust optical depth to loadings fields, see Table 3. The MEE depends on the modelled dust particle size distribution (in particular the presence of large particles) but with a significantly smaller inter-annual variability than dust optical depths and loadings. This fact explains the use of MEE for ad-hoc relationships between dust optical depths and loadings with a constant factor (Pu and Ginoux, 2018b).

10   Based on the histogram of the annual global values of dust optical depth we estimated the distribution for each model based on a kernel density estimation. The results shown in Figure 4 (bottom left panel) indicate the presence of two main groups for our model ensemble on the one centered around a value close to 0.01, and the second one around 0.025, a value closer to the proposed constraint. The solid black line shows the distribution of dust optical depth at 550 nm for a annual sampling

15   with a kernel density estimation, and how it compares with the distribution proposed by Ridley et al. (2016) and AeroCom Phase I median value. The EC-Earth model agrees actually in both central value and typical inter-annual variability (as represented by the width of the distributions). These results should be also interpreted in the context of the total aerosol optical depths, Figure 4 (bottom right panel). We observe that the UKESM has lower values of dust optical depth but actually the

20   largest values of total aerosol optical depth, with similar global mean values to those obtained by MODIS at 550 nm but with a narrower distribution. The EC-Earth model has AOD values slightly smaller than MISR estimates with similar inter-annual variations.

Aside from the CNRM-6DU model, all models have values of dust loadings smaller than 20 Tg with NorESM at about half of the ensemble median value. This agrees with the AeroCom Phase

25   I models where the fine dust dominates the total loads with ensemble value of 15 Tg. The MEE multi-model median reported by Huneeus et al. (2011) is 0.72 $\mathrm{m}^2\mathrm{g}^{-1}$, similar to the global MEE value of 0.6 $\mathrm{m}^2\mathrm{g}^{-1}$ used by Pu and Ginoux (2018b) to compared DOD and dust loadings of CMIP5 models. Recently, Adebiyi et al. (2020) estimated a mean over 13 observational stations giving a values slightly smaller than 0.6 $\mathrm{m}^2\mathrm{g}^{-1}$. Our estimation of MEE shows that EC-Earth and NorESM

30   depart from that value, whereas the other models remained close reasonably to (Pu and Ginoux, 2018b) hypothesis and AeroCom median value.

We note that the global mean values for the models, as shown in Figure 4 (top panel) are partially conditioned by ocean or land regions with low dust loadings. To complement this analysis, we present two additional comparisons in the supplementary material. The first is shown in Figure

35   GL1, for the case when only values over land are considered. The second is shown in Figure GL2

for the case when the annual values are estimated over the dust belt that covers most of the Sahara and the Middle-East. Both Figures still indicate important differences between models. Recently, Adebiyi and Kok (2020) proposed that the total load of dust in the atmosphere is higher than typical estimation and give a mean value close to 30 $\mathrm{Tg\,yr}^{-1}$, where the contribution of coarse mode is

5 more important than the fine mode. In this case the estimation of CNRM-6DU model would be the most accurate of the CRESCENDO-ESM in terms of total mass of mineral dust in the atmosphere.

A specific PDN experiment with the IPSL model was run for 5 years (2010 to 2014) to analyze how the representation of the dust size distribution influences the dust cycle. In this simulation , named IPSL-4DU, the dust scheme is based on 4 dust insoluble modes covering the whole range

10 of sizes from 0.1 to 100 μm and nudged winds were used. The results shown in the Table GL.7 are consistent with the impact of larger particles on dust emissions and loadings in UKESM and allow us to discuss the role of each mode independently. The total emissions for IPSL-4DU are dominated by larger particles of mode m_{22} but are promptly removed from the atmosphere through their sedimentation which is very rapid. When comparing the total load for each mode, actually

15 the coarse size mode $m_{2.5}$ is more abundant than m_{22}. Amongst all the modes, mode m_7 has the largest contribution, with 2/3 of the total, which is comparable to the large particles represented in the CNRM-6DU model, consistent with Adebiyi and Kok (2020). Note that the dust loads in CNRM-6DU model are larger than in CNRM-3DU, albeit similar emissions. The explanation for this difference is that the bin that includes particle sizes from 1.25 to 10 μm in CNRM-3DU is split

20 into different bins in the CNRM-6DU model, which have different life times in the atmosphere. In contrast to emissions, optical properties are dominated by the contributions of accumulation to coarse size particles compared to the largest particles of mode m_{22} that does not play a large role in its contribution to aerosol extinction. Those values are then used for assessments about modal contributions to direct radiative effects.

25 Mineral dust aerosol interaction with solar and terrestrial radiation results in both absorption and scattering of light. These interactions are strongly dependent on dust mineralogical composition and particle size distribution, hence they differ regionally (Ginoux, 2017; Kok et al., 2017). We estimated the respective roles of the different modes (that represent different particle sizes ranges), we remind that in the case of multi-modal distributions the estimations of direct radiative effects (DRE) by

30 each mode is, somewhat non-linear (Biagio et al., 2020). This is illustrated when the sum of the contribution of the DRE from each mode is not exactly equal to the multi-modal dust contribution. The Appendix A show how, with an estimation of DRE per mode based on the combination of two different methods, we ascertained modal values of DRE that combine close to the multi-modal DRE estimation. This is summarised in Table 6 where the estimations per-mode DRE for each method are

35 shown together the their mean. The sum of these mean values per mode is now consistent with the
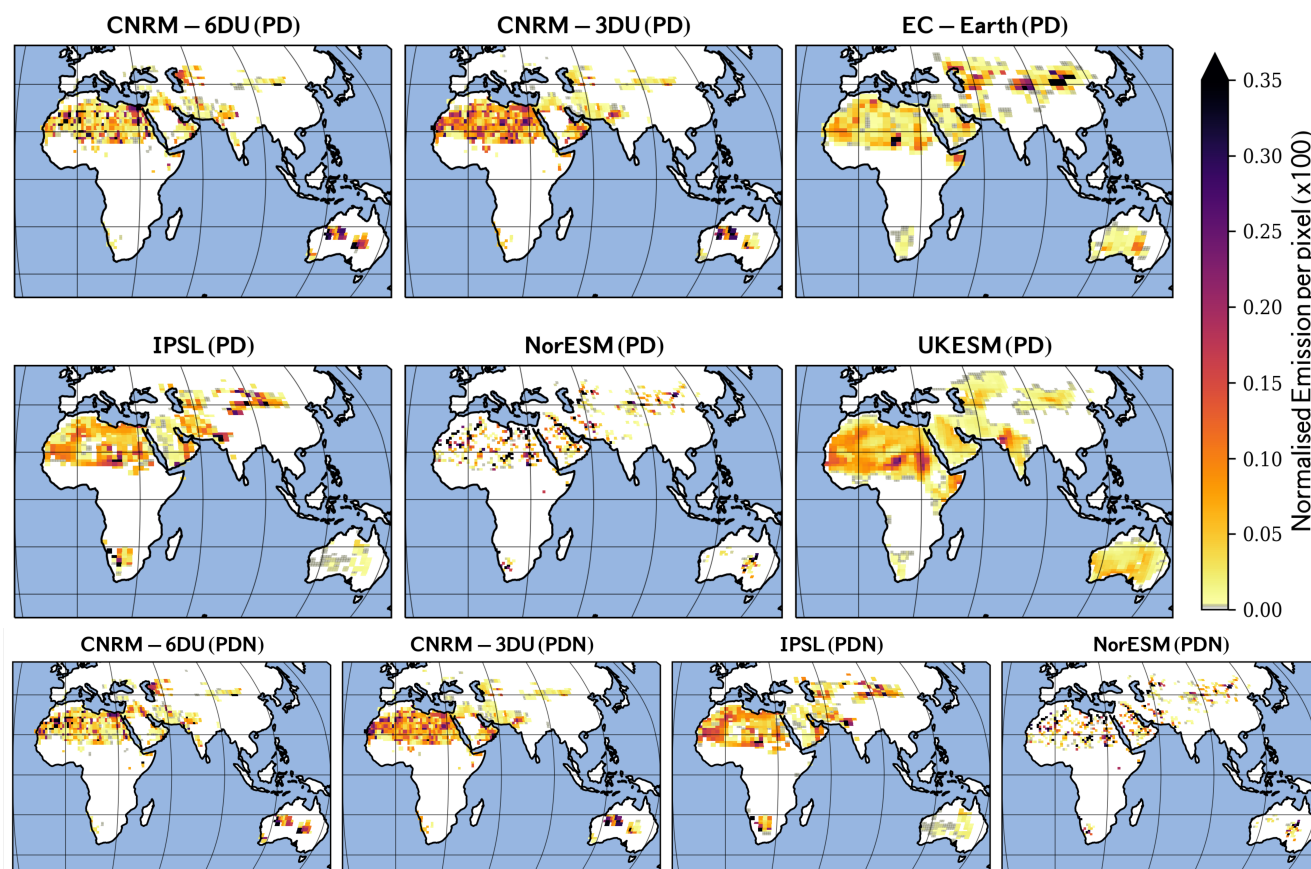
Figure 7. Normalized map of emissions (x100) over NorESM grid resolution. On the top: experiment with present day aerosol and chemistry forcings (PD), on the bottom the PDN experiment. We used a conservative near-neighbour interpolation to create emission maps that preserve global values on higher resolutions, then the maps were normalized to have a common comparison scale. The color-bar represents the normalized emission tendencies per grid with range [0,100]. The figure S.E5 is the analogous of this figure for PI experiment.

multi-modal DRE. It is remarkable how the estimations of TOA-SW for m_7 by each method differ by a factor 2. The non-linear effects in the surface at the SW are also important with differences in the sum of the 4 modes between methods of $0.3\ \mathrm{Wm}^{-2}$.

The analysis of direct radiative effects (DRE) by mode, shown in Table 6, indicates that the largest particles (mode m_{22}) have a minor impact on the DRE in both LW and SW. In contrast, the inclusion of the mode with the smallest particles contributes to the SW cooling although it is the coarse size mode the one that dominates the net direct radiative effects at the top of the atmosphere. At the surface however, the mode m_7 has the largest effect on both SW and LW but its net contribution (LW+SW) is smaller than the coarse mode $m_{2.5}$.

5.2 Dust global spatial patterns

Figures 5 and 6 describe temporal mean properties of dust in CRESCENDO ESMs (PD simulations) over the 15 years. Models that have a sectional representation of the DPSD (CNRM-6DU, CNRM-3DU and UKESM) are shown in Figure 5. For all these models, emission and dry deposition show strong spatial correlations because gravitational settling of large particles is happening close to dust sources, whereas wet scavenging dominates the deposition process over the oceans. The extension of regional emissions over Sahel and Somalia is more pronounced for UKESM than for CNRM models. Although the Chalbi Desert in Kenya is also a location for emission in the CNRM models, the extent over which emissions occur in the UKESM is significantly larger. The figure also suggests differences in deposition for the CNRM models: CNRM-3DU model has higher values of dry deposition than CNRM-6DU but the opposite is true for wet deposition. These differences in wet deposition are pronounced over the North Atlantic and the Indian Ocean. In contrast, wet deposition is more intense over the Sahel and the Indian sub-continent in the UKESM model which indicates the strong role of the monsoon at scavenging dust. It is also noticeable that the CNRM-3DU annual mean wet deposition decreases from West to East over the Indian Ocean while the inverse is true for UKESM. Despite systematic smaller values for UKESM optical depth compared to CNRM-3DU, they have rather similar spatial distributions.

Models with a modal description of the DPSD (IPSL, EC-Earth3-AerChem and NorESM) are shown in Figure 6. Dust emissions from EC-Earth are more intense in Asia than other for models whereas EC-Earth has the smallest emissions from the Northern Sahara. This causes the trans-Pacific transport of dust to peak in this model compared to others, and the transport across the Atlantic to be smaller. Northern Sahara emissions from NorESM are more localized but with larger peak values. Like for sectional models, dry depositions correlates well spatially with emissions whereas wet deposition dominates over oceanic regions. EC-Earth shows both larger wet deposition and optical depth over East Asia extending into the Sea of Japan. For all models with a modal scheme,

Table 8. Total wet depositions [Tg yr^{-1}] for Present Day (PD) simulations. Over oceanic-regions, see Figure 2. The numbers in brackets indicate the order rank in contributions by region from the highest to the lowest one. The equivalent Tables for PI and PDN experiments are in supplement: tables D1 and D2, respectively.

	CNRM-6DU (PD)		CNRM-3DU (PD)		EC-Earth (PD)		IPSL (PD)		NorESM (PD)		UKESM (PD)	
Global Earth	2108.9		753.8		493.2		968.3		275.7		949.8	
Land	1397.1		541.3		272.9		575.7		203.9		673.6	
Ocean	711.8	(33%)	212.5	(28%)	220.3	(45%)	392.6	(40%)	71.8	(26%)	276.1	(29%)
North Atlantic	207.4	(1)	65.4	(1)	61.7	(2)	156.1	(1)	23.7	(1)	103.4	(1)
South Atlantic	9.1	(6)	5.1	(5)	14.6	(5)	47.0	(2)	2.5	(4)	11.3	(4)
North-Indian Ocean	187.2	(2)	47.8	(2)	16.6	(4)	36.5	(4)	16.2	(2)	33.1	(3)
South-Indian Ocean	39.3	(4)	13.9	(4)	4.1	(6)	18.5	(5)	2.4	(5)	11.1	(5)
Pacific East	93.6	(3)	21.1	(3)	70.5	(1)	39.1	(3)	7.3	(3)	41.5	(2)
Pacific North-West	2.9	(7)	0.2	(8)	21.0	(3)	12.2	(6)	1.0	(6)	10.2	(6)
Pacific South-West	9.9	(5)	2.5	(6)	3.0	(7)	3.8	(8)	0.9	(7)	5.9	(7)
Antarctic Ocean	5.4	(8)	2.2	(7)	2.5	(8)	7.3	(7)	0.6	(8)	4.3	(8)
Ocean. North. Hemis.	569.1		162.9		188.5		287.4		59.2		218	
Ocean. South. Hemis.	142.1		49.5		31.8		104.2		12.5		58.1	

Table 9. Total dry depositions [Tg yr^{-1}] for Present Day (PD) simulations. Over oceanic-regions, see Figure 2. The numbers in brackets indicate the the order rank in contributions by region from the highest to the lowest one. The equivalent Tables for PI and PDN experiments are in supplement: tables D3 and D4, respectively.

	CNRM-6DU (PD)		CNRM-3DU (PD)		EC-Earth (PD)		IPSL (PD)		NorESM (PD)		UKESM (PD)	
Global Earth	1283.9		1708.1		633.5		590.6		1092.5		6566.3	
Land	1068.6		1487.9		555.8		523.1		986.6		6366.1	
Ocean	215.4	(16%)	220.2	(13%)	77.7	(12%)	67.5	(11%)	105.9	(10%)	199.4	(3%)
North Atlantic	74.2	(1)	88.6	(1)	31.7	(1)	31.6	(1)	28.4	(2)	81.9	(1)
South Atlantic	1.4	(6)	4.9	(4)	2.3	(4)	5.3	(3)	2.5	(4)	1.9	(5)
North-Indian Ocean	67.7	(2)	56.4	(2)	14.3	(2)	13.8	(2)	49.5	(1)	51.3	(2)
South-Indian Ocean	16.2	(3)	16.7	(3)	1.4	(7)	0.9	(6)	0.8	(6)	9.1	(4)
Pacific East	15.2	(4)	9.7	(3)	13.3	(3)	2.3	(5)	3.9	(3)	12.5	(3)
Pacific North-West	0.2	(7)	0.3	(6)	2.2	(5)	2.7	(4)	0.9	(5)	1.5	(6)
Pacific South-West	3.0	(5)	2.7	(5)	0.4	(7)	0.5	(7)	0.6	(7)	0.6	(7)
Antarctic Ocean	0.1	(8)	0.1	(7)	0.2	(8)	0.3	(8)	0.1	(8)	0.4	(8)
Ocean. North. Hemis.	175.8		177.3		71.3		58.3		98.6		172.4	
Ocean. South. Hemis.	39.5		42.8		6.4		9.2		7.3		26.9	

wet deposition over the Indian ocean is mostly occurring over its Western part. Analogous of Figures 5 and 6 but PI and PDN experiments are shown in Figures S.GL.3 and S.GL.4 for PI and Figures S.GL.5 and S.GL.6 for PDN.

5.3 Dust emissions

The dust emission rate is defined as the surface mass flux of mineral dust in the vertical direction F_d. This flux is derived in climate models as a function of surface winds but there are different schemes depending on the complexity of the description. Shao and Dong (2006) classify all dust emission

5 schemes in three different categories named α, β and γ schemes. The α-schemes are those where F_d is directly described in terms of the wind speed (with a non-linear function including a friction velocity threshold) with an imposed empirical size distribution at emission. IPSL-INCA uses this approach. The β-schemes instead estimate the vertical flux from the dust horizontal mass-flux which itself can be parameterized depending on a geographical erodibility factor and the surface wind.

10 Although this erodibility factor depends on soil properties and moisture, sub-daily global patterns of dust emission are tightly correlated with wind fields, and therefore with the atmospheric general circulation (Shao et al., 2011). Examples of β-schemes are those described by (Zender et al., 2003) and (Woodward, 2001b) that are used respectively by NorESM and UKESM models. But also the EC-Earth model whose horizontal flux is estimated with the scheme described by Marticorena and

15 Bergametti (1995) which distributes particles in four bins with values up to 8 μm. Those values are mapped in the modes described in the Table S.MD.9. Similarly the CNRM models have a drag partition according to Marticorena and Bergametti (1995) but the size distribution at emission follows that defined at (Kok, 2011). The γ-schemes aim to describe the physical process driving the size resolved vertical flux but they require additional information of underlying soil properties and are

20 not used by CRESCENDO-ESM.

Despite the different schemes all of them agree that regions where most dust is uplifted are subtropical arid and semi-arid regions. Such regions are characterized by atmospheric stability and scarce rainfall. This global pattern is however modulated by the Inter-Tropical Convergence Zone (ITCZ) oscillations, monsoons, and orography, as visible in Figures 5 and 6. Because the Himalayan

25 mountains filter the water-vapor transport from then Indian Ocean all the models have important dust sources in Northern Asia (such as the Taklamakan and Gobi deserts) but the specific location of Asian sources, and their relative contribution to global emissions differs significantly between models.

Nowadays we understand how regional climate influences the dust emissions and its variability,

30 together with the atmospheric systems linked to dust emission episodes. But dust emission modelling still constitutes an active research field (Shao, 2008). In particular, the dust particle size distribution (DPSD) at emission is critical for a better description of the global dust cycle (Mahowald et al., 2014) but its modelling need to be improved for three main reasons: first because there is not an unified approach; second because there are discrepancies in the role of wind speed at emission for

larger dust particles (Alfaro et al., 1998, 1997); and third, because the quantitative link between soil properties and dust emission fluxes still need additional research.

Despite the several set of parametrizations of DPSD at emission (Kok, 2011; Alfaro and Gomes, 2001; Shao, 2001, 2004) the modeling of dust in global climate models is highly influenced by a

5 balance of the different elements involved (vertical flux at small scale, soil erodibility, wind fields), which explains that during last decade the estimation of dust emissions when online coupled with meteorological fields have improved their results significantly. On one side the modelled wind surface friction velocity and speed agree better with actual meteorological conditions, and on the other side the description of the soil surface properties has become more accurate.

10 All those facts explain why the comparison (Table 7) of the emissions (PD experiment) over large regions is fairly consistent among models: they agree on the main source of mineral dust located in the Sahara desert but representing, from 39% of total global emissions in the EC-Earth model to 66% CNRM-3DU. Previous studies (Shao et al., 2011) estimated the contribution of Africa to dust emissions on a range from 50% to 68% but also including Namibia Desert emissions. The

15 consistency is larger when we considered larger regions like hemispherical contributions where all the models show emissions beyond 85% in the Northern Hemisphere. When smaller regions are considered, the differences in relative contributions between models increase, which is also expected when turbulence at small scale and/or convection (Allen et al., 2015) plays a role in dust events. If we evaluate total values rather than relative contributions, the driving factor to explain differences

20 between modelled emissions relies in the upper threshold of particle sizes at emission.

Dust emissions by regions (which are shown in Figure 3) and their intensities (in $\mathrm{Tg\,yr}^{-1}$) are listed in Table 7 for the PD experiment. The most intense source of dust for the EC-Earth model is located over the Gobi Desert, while North Sahara, a key emitting region in all other models, constitutes only the 4th most intense region in emissions (after the Taklamakan and the Kyzyl-Kum).

25 The Bodele is remarkably an important dust source across all CRESCENDO ESMs. As expected from the analysis of dust optical depth over Asian regions: the Taklamakan, Kyzyl Kum and Thar deserts exhibit substantial differences. Regarding UKESM, it has an additional and extended dust source over the Somalia Desert (see Fig. 5) which is only a relatively small source in other models. The analogous Tables of 7 can be found for PDN and PI experiments in Tables S.DE.1 to S.DE.4,

30 showing similar model differences.

If we want to compare realistically global climate model emissions over smaller regions, we need to account for the different model resolutions. We opted to display normalized emissions estimations over a common grid for all the models. Our method interpolates the emission flux from each model grid to that with the highest spatial resolution (NorESM). We use a near-neighbour interpolation

35 method which conserves the flux in each model when compared to the flux integrated over the orig-
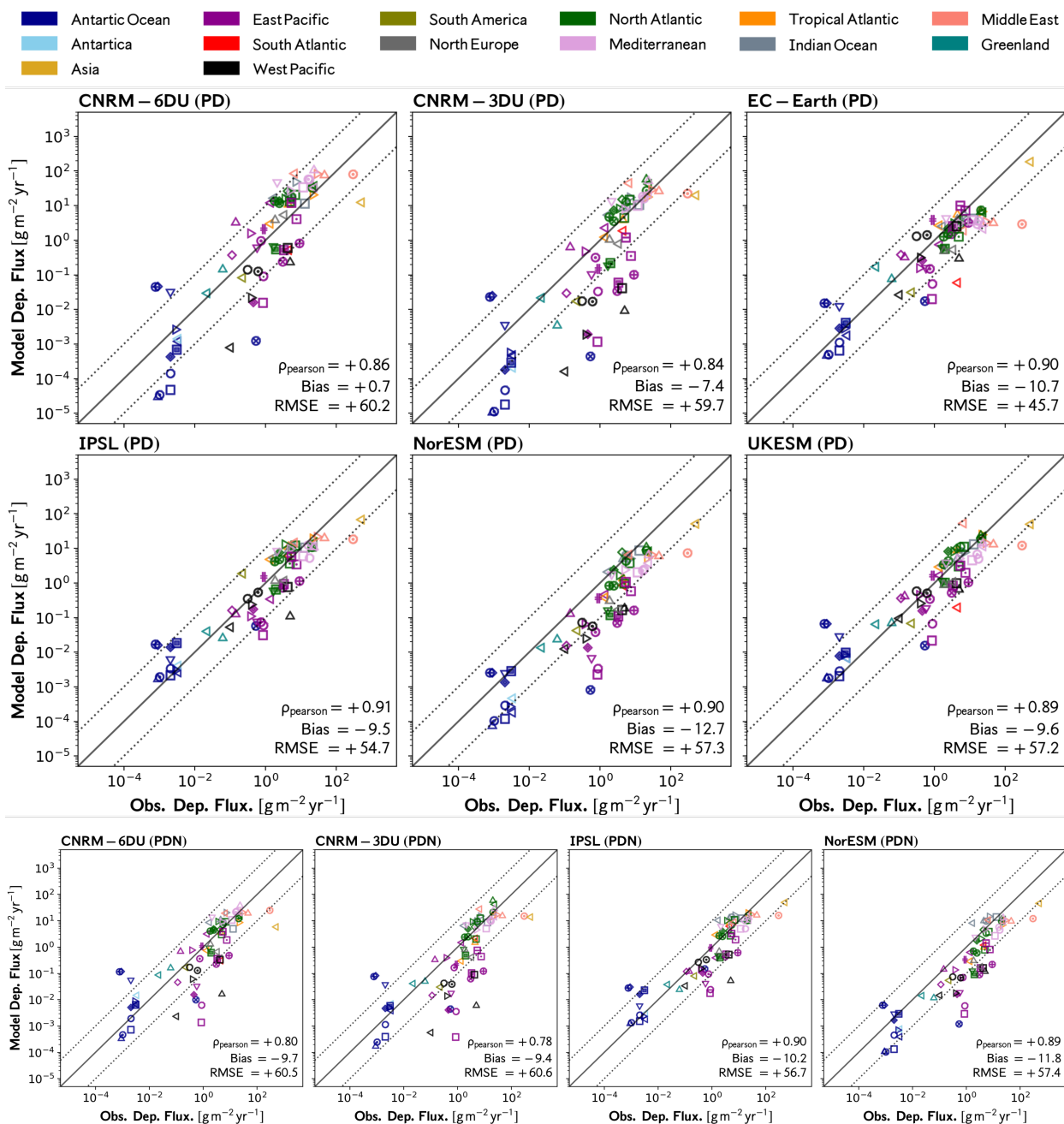
Figure 8. Comparison of estimated total annual deposition flux with CRESCENDO ESMs with the dataset presented at (Huneeus et al., 2011), whose stations are mapped in Figure 1 (left panel). The model values taken are those from the PD experiment (top part) and PDN experiment for bottom row. Figure S.D11 is the analogous of this figure but for the PI experiment.

inal model resolution. This method is not introducing any ad-hoc information on how the emission tendency is distributed within the original grid-pixel. A monthly time-series of normalized emitted dust mass per grid-pixel, with respect to global monthly emissions, is produced using this method. These normalized emissions over a common grid allow us to pick up differences over spots that

5   are caused either by the formulation of the source function or by the dust particle size distribution imposed during the emission process.

A direct comparison of dust emission maps with observations is challenging because it would require to translate the observed frequency of dust events into a dust emission flux rate (Evan et al., 2015). Assuming the hypothesis of Evan et al. (2015) for this mapping, the hot spots of their SE-

10 VIRI emission normalized product can be compared with our normalized maps (in terms of relative contribution of different pixels over North Africa). In particular they suggest that beyond Bodele Depresion an important source is at Hoggar Mountains (west of Bodele Depression). This feature is only captured by CNRM model.

The annual average of these monthly maps is presented in Figure 7 for PD and PDN experiments.

15 The models CNRM-6DU and CNRM-3DU show similar values per grid-cell, which indicates the use of the same information on soil properties, but the normalized emissions although similar are not identical, reflecting the differences in dust size distribution at emission. In these models, the normalized emissions over Australia are higher than for other models, and this difference is also appearing in the optical depths simulated at the AERONET station of Birdville. The description of

20 semi-desert areas in Northern India has many similarities to the IPSL model. Emission tendencies from the UKESM model extend to areas where other models do not simulate emissions, and the pattern of emissions is more smooth. In particular, significant emissions occur over Sahel, Ethiopia, Somalia, and over India. For these regions, higher dust emissions in UKESM could have a stronger impact on African and Asian monsoons. The more granulated pattern is found for the NorESM

25 model, which is because of the higher resolution of the source functions implemented. The last row in Figure 7 corresponds to the normalized emission maps for PDN experiment, they indicate that although there are important differences between PD and PDN experiments in terms of total emissions, the spatial pattern of emissions are similar once they are normalized. We can ascertain this fact by comparing the CNRM-6DU normalized emission maps for PD and PDN experiment.

30 The study for the PI experiment is in the supplementary information: figure S.DE.5.

5.4   Dust deposition

Previous studies (Huneeus et al., 2011; Albani et al., 2014) show that total deposition of dust, when compared with in-situ measurements, agree globally only within a factor ten. Part of the reason is
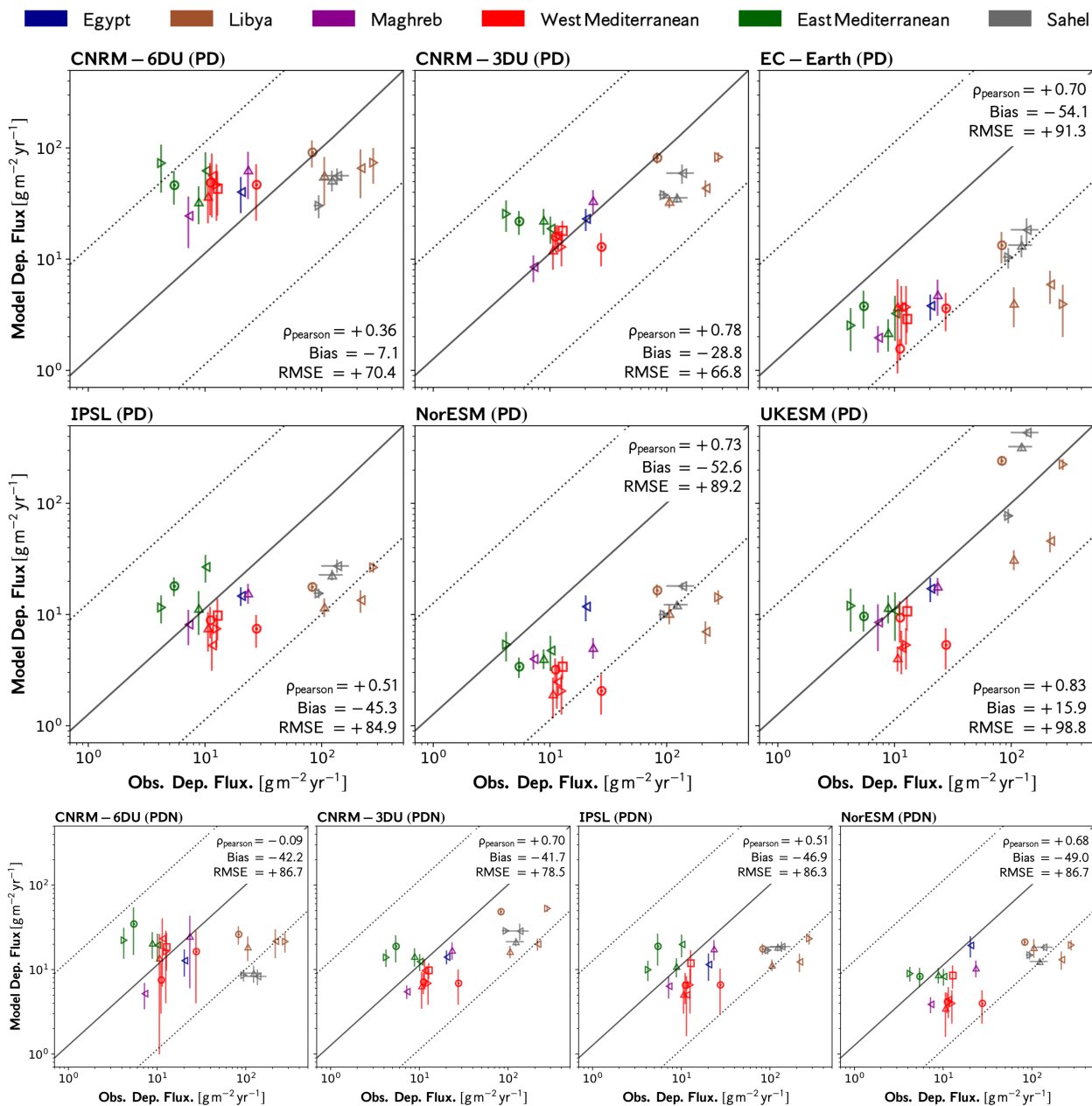
Figure 9. Comparison of estimated total annual deposition flux with CRESCENDO ESMs with the dataset stations shown at Figure 1 (right panel). The model values taken are those from the PD experiment (top part) and PDN experiment for bottom row. Figure S.D.11 of the supplement is the analogous of this figure but for the PI experiment. Vertical bars on the bottom panel represent the year to year internal variability captured by each model. The grey horizontal bars displayed for the Sahel stations represent the year to year variations in the observations.

Table 10. Statistical properties of the comparision of the CRESCENDO-ESMs total deposition against the network-SET-M (see Figure 1 panel b). Statistic metrics used in this table are described on Table 4,Pearson Correlation Coefficient (ρ), bias (δ), normalized bias (δ_N), Ratio standard deviations (Σ), Normalized mean absolute error (θ_N) and Root mean square error (RMSE=η).

Model	Exp.	Deposition Network-SET-M					
		ρ	δ	δ_N	Σ	θ_N	η
CNRM-6DU	PD	+0.08	-20.18	-0.34	+0.30	+0.90	+77.75
CNRM-3DU	PD	+0.34	-45.16	-0.76	+0.15	+0.85	+84.72
EC-Earth	PD	+0.70	-54.12	-0.91	+0.06	+0.91	+91.26
IPSL	PD	+0.51	-45.25	-0.76	+0.09	+0.83	+84.90
NorESM	PD	+0.68	-52.10	-0.87	+0.07	+0.88	+89.01
UKESM	PD	+0.40	-49.91	-0.84	+0.10	+0.86	+87.82
CNRM-6DU	PDN	-0.08	-53.43	-0.90	+0.08	+0.92	+91.78
CNRM-3DU	PDN	+0.29	-54.32	-0.91	+0.07	+0.93	+91.61
IPSL	PDN	+0.51	-46.90	-0.79	+0.07	+0.84	+86.30
NorESM	PDN	+0.62	-48.49	-0.81	+0.07	+0.83	+86.73

that dry and wet deposition depend on the dust particle size distribution, whose representation is challenging for current global climate models.

Processes driving dry deposition such as turbulent motions of particles and gravitational settling are both particle size dependent, as the aerodynamic resistance and the terminal velocity due to

5   friction depend on the effective dust particle diameter. Wet deposition on precipitation events also depends on the size of the particle (Seinfeld and Pandis, 1998) but measurements of aerosol lifetimes below clouds are scarce. Furthermore, other aerosol processes inside clouds modify the aerosol size distribution as well as their optical properties essentially due to potential aggregation of water-coated aerosols (Mahowald et al., 2014).

10   As the gravitational settling of large particles is dominant close to dust sources, regions remote from the main emission sources are well suited to compare models with different emission schemes, and evaluate their respective total dry and wet deposition. Close to dust sources the upper threshold on the emitted dust particle sizes plays a role in the comparison with measurements. In particular, wet deposition over oceanic regions is enhanced relative to dry deposition which motivates targeting

15   these specific regions for comparison. Tables 8 and 9 show the regional analysis of wet and dry deposition (including the sedimentation/gravitational settling) over oceans. These results are globally consistent with those shown by Shao et al. (2011). The two main oceanic regions where dust deposition occurs are the North Atlantic and the Indian Ocean even though EC-Earth model simulated the largest dust wet deposition over the East Pacific Ocean. For all models, the fraction of dry and

20   wet deposition over ocean is smaller than over land. Wet deposition over oceans represents 40% and

Table 11. Statistical properties of the comparision of the CRESCENDO-ESMs total deposition against the network-H2011 (see Figure 1 panel a). Statistic metrics used in this table are described on Table 4. Pearson Correlation Coefficient (ρ), bias (δ), normalized bias (δ_N), Ratio standard deviations (Σ), Normalized mean absolute error (θ_N) and Root mean square error (RMSE=η).

Model	Exp.	Deposition Network-H2011					
		ρ	δ	δ_N	Σ	θ_N	η
CNRM-6DU	PD	+0.86	+0.70	+0.05	+0.41	+1.26	+60.15
CNRM-3DU	PD	+0.84	-7.36	-0.48	+0.22	+0.89	+59.73
EC-Earth	PD	+0.90	-10.71	-0.70	+0.36	+0.73	+45.74
IPSL	PD	+0.91	-9.54	-0.62	+0.16	+0.78	+54.69
NorESM	PD	+0.90	-12.68	-0.83	+0.11	+0.84	+57.26
UKESM	PD	+0.89	-9.58	-0.62	+0.16	+0.81	+57.21
CNRM-6DU	PDN	+0.80	-9.72	-0.63	+0.13	+0.84	+60.52
CNRM-3DU	PDN	+0.78	-9.44	-0.62	+0.18	+0.88	+60.60
IPSL	PDN	+0.90	-10.23	-0.67	+0.13	+0.79	+56.67
NorESM	PDN	+0.89	-11.80	-0.77	+0.11	+0.83	+57.42

45% respectively of the total wet deposition for IPSL and EC-Earth. But for NorESM it represents 26% of the global wet depositions. Dry deposition over oceans ranges from 3% to 16% of global dry depositions. For the UKESM model, the dry deposition over land is 97% of the total dry deposition, due to the gravitational settling of large particles close to emission regions. Tables 8 and 9 also show

5 higher consistency in the total dry deposition over oceans in the model ensemble (from 67 to 215 in $\mathrm{Tg\,yr^{-1}}$) that in the wet deposition (72 to 712 in $\mathrm{Tg\,yr^{-1}}$). Results for PDN and PI experiments are included in Tables S.DD.1 to S.DD.4

5.4.1 Network of Dust deposition observations

Figure 8 shows the total annual deposition for PD and PDN experiments for the locations shown in
10 panel (a) of Figure 1, and Figure 9 shows the total annual deposition for PD and PDN experiments for the locations shown on panel (b) Figure 1. Figures Dep.11 and Dep.12 show the analogous for the PI experiment. Qualitatively the global results are similar to Huneeus et al. (2011) where at most of the stations the modelled deposition is within a factor of 10 of the observed deposition flux (in the figures, the region between the dotted lines) As a consequence the estimated Pearson correlation
15 of deposition flux calculated over log-values for the full network shows a reasonable value for all models.

All the models agree that Antarctica and Southern Ocean has the lower values of total deposition. However, UKESM and IPSL tend to slightly overestimate the total flux whereas CNRM models tend to underestimate the flux (with also a larger range of total deposition values than the range re-
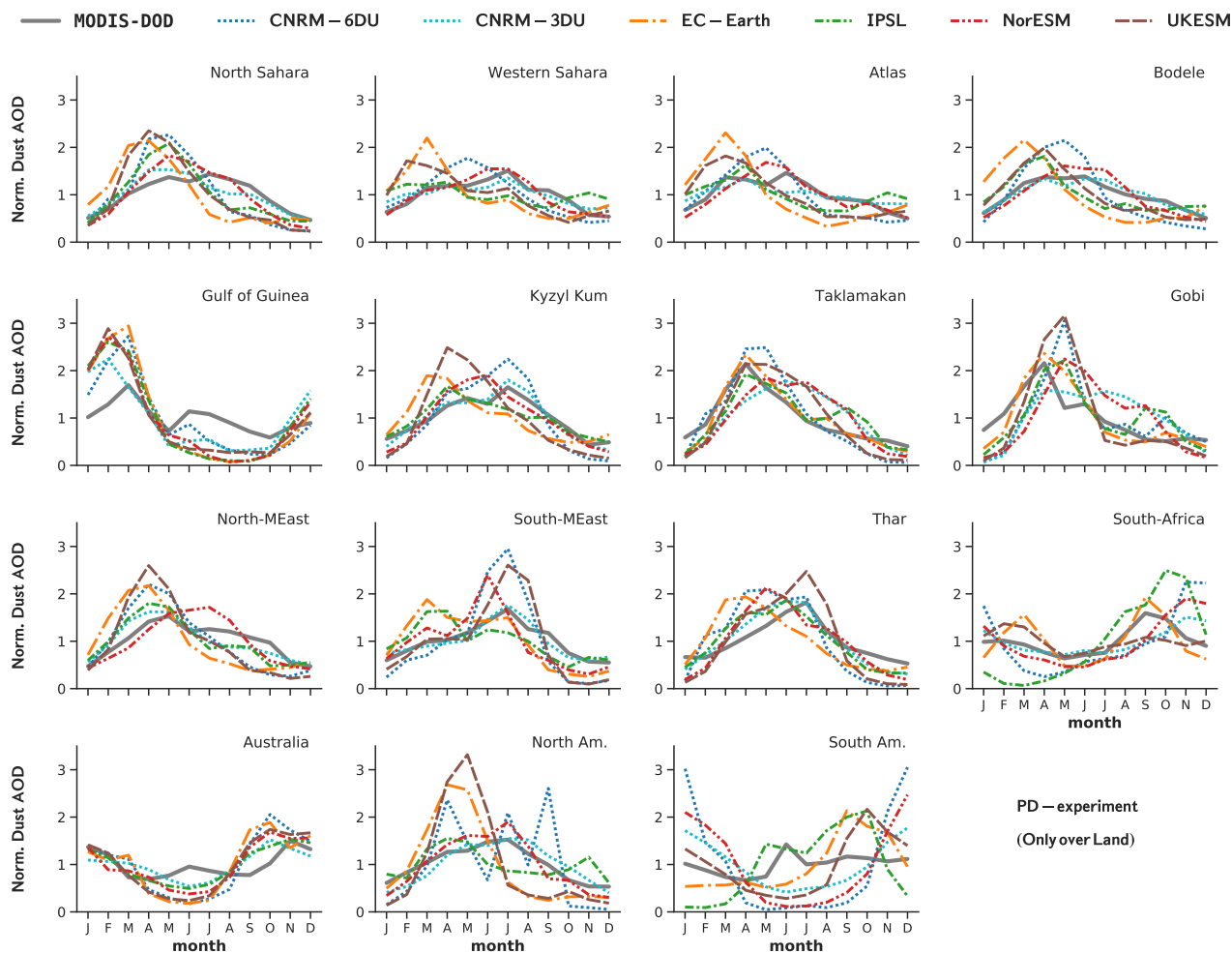
Figure 10. Seasonal cycle relative to the annual mean value of Dust Optical Depth as modelled by CRESCENDO ESMs over 15 regions. These seasonal cycles are compared against the DOD product of derived dust optical depth over land based on MODIS deep-blue retrievals (Pu and Ginoux, 2018b), see supplementary information for the description of how these products are derived and the analogous of this figure for PDN and PI experiments.

ported by the observations). This is consistent with the semi-Lagrangian model implemented in their dynamical core which is expected to underestimate deposition fluxes mainly at distant regions for dust sources. Regarding the Pacific region closer to North America (named West Pacific) NorESM, CNRM-6DU and CNRM-3DU tend to underestimate the deposition. In the case of East Pacific re-

5   gion NorESM systematically underestimate deposition flux. Regarding CNRM models the underestimate the total deposition over the north hemisphere part of East Pacific but not in the southern part of East Pacific due to the enhanced emissions of these models over Australia deserts. All the models but the EC-Earth model underestimate the deposition over the Asia station, also the EC-Earth model report good values of total deposition over the northern East Pacific as it has the largest relative con-

10 tributions over Gobi desert between all the models. All the models show a good agreement on the Atlantic region (both North and Tropical regions) and Middle East although UKESM and EC-Earth model underestimate the values in the station in the South Atlantic. The deposition fluxes over the Indian ocean are fairly well described by all models.

If we compare the observations against the model total depositions obtained from the experiment

15 with nudged winds (last row in Figure 8 the correlation coefficients are similar, but differences between models are reduced, specially for the CNRM models. This is illustrated in Table 11 with a negative bias for all models (from -9.4 to -11.8), and the ratio of standard deviations Σ range between 0.11 and 0.18 (for PD experiment between 0.1 and 0.41).

In Figure 9 we analyze the ability of ESMs to reproduce deposition fluxes regionally and closer

20 to sources (for PD and PDN experiments). We focus on the Mediterranean Sea and include three additional stations over the Sahel. The analysis reveals that only the UKESM model reproduces the full range of observed deposition fluxes. All the other models underestimate total depositions fluxes over stations where fluxes exceed $100\,\mathrm{g\,m^{-2}yr^{-1}}$, and only the CNRM-3DU model estimates well the observed dust deposition in the northern Mediterranean Sea. Over the Sahel region, CNRM

25 models and UKESM provide reasonable values of total deposition flux, but UKESM overestimates the inland depositions, whereas the other models provide more consistent bias over the whole region. The Sahel stations are including horizontal bars describing the inter-annual variability over the mean values, which can be compared with vertical bars describing the variability in the models. In this case EC-Earth is the model that captures best the year-to-year over mean values of dust deposition

30 flux over the inland Sahel stations. For West Medierranean the CNRM-3DU has the smallest bias, whereas in the full Mediterranean region UKESM and IPSL perform well in terms of global bias. EC-Earth and NorESM underestimate close to source total depositions consistent with the cutoff in size larger than 8 μm the emitted particles, and CNRM-6DU overestimates the depositions on the whole Mediterranean region. For the experiment with nudged winds, we observe a better consistency

35 between models showing all of them similar values of total deposition of the different sub-regions.
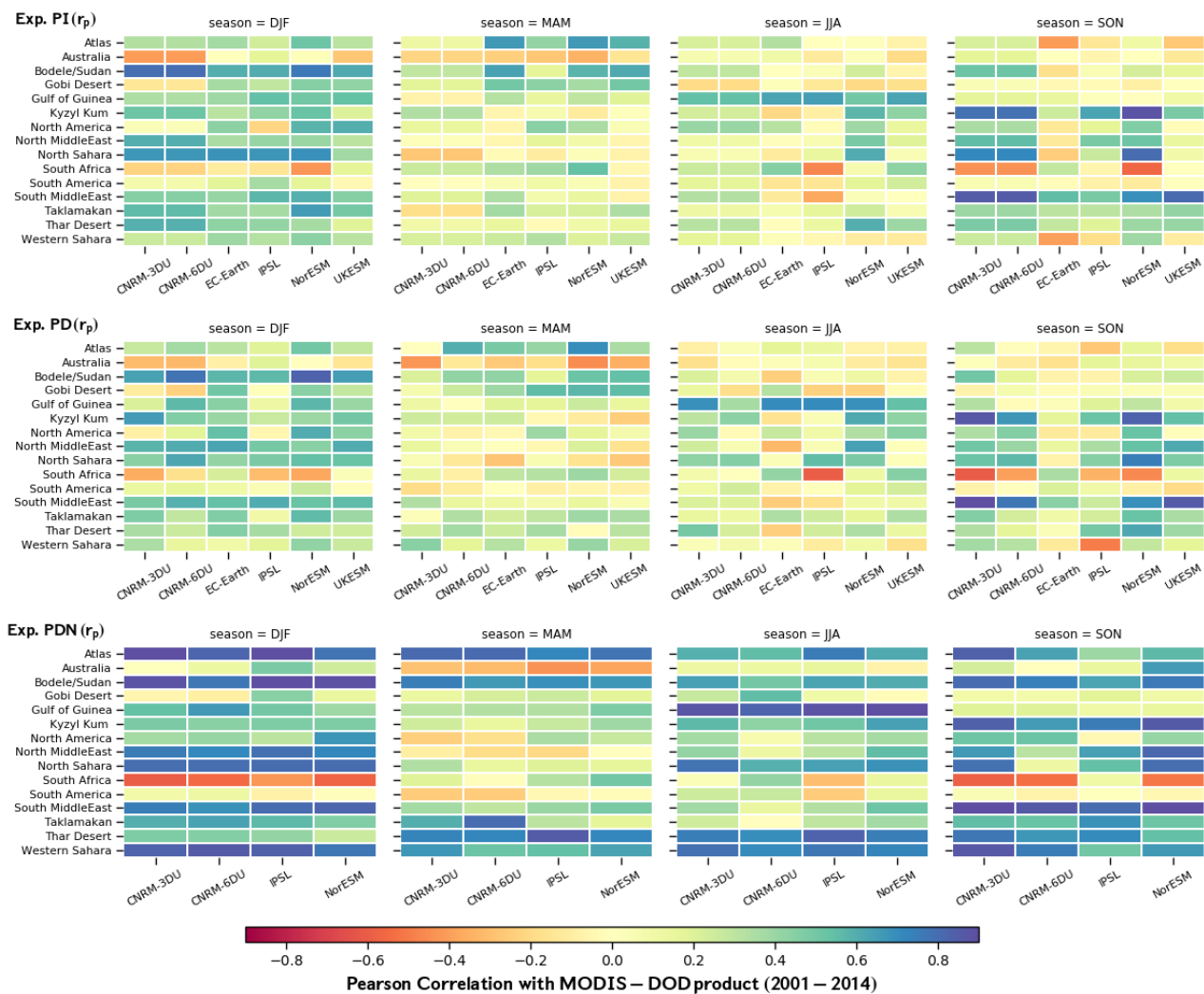
Figure 11. Skill of CRESCENDO-ESMs by regions calculated as the Pearson correlations between the ESM time-series of dust optical depth for each season and that from MODIS-DOD. The time interval spans from 2001 to 2014. It assess the performance of the different models to reproduce the inter-annual variability of each season against observations over dust source regions.

However this implies an understimation over Sahel for CNRM-6DU model that also has the largest interannual variability over the West-Wediterranean. The statistics metrics are shown in Table 10.

5.5 Dust optical depth

The simulated dust optical depth (DAOD) by climate models has been compared previously with
5 those retrieved through a network of ground-based sun-photometers (Huneeus et al., 2011) but also with products derived from satellite retrievals (Pu and Ginoux, 2018b; Peyridieu et al., 2013). There are also inter-comparisons between global climate models (Shindell et al., 2013). The overall agreement reported by these studies between retrieved and simulated aerosol optical depth is within a factor of two. Those results support the reliability of global estimations of the radiative effect from
10 mineral dust. However, given that it is a vertically integrated parameter, it masks larger differences present in partial columns estimations.

Our study focuses first on the comparison in regions defined in Fig. 3. We compared the DOD of the CRESCENDO ESMs with satellite, as well as inter-compare simulated dust optical depth. Figure 10 shows the seasonal cycle (relative to the annual mean value of each model) and the MODIS DOD
15 product during the period 2001-2014, for the PD experiment (the PDN and PI experiment are shown in Figures S.DOD.1 and S.DOD.2). We can hence analyse the seasonal amplitude relative to the annual background signal per region for each model. Figure S.DOD3 shows the direct comparison of the seasonal cycle without relative values.

Over the most prominent preferential dust source regions (first row of Figure 10), the amplitude
20 of the seasonal variability is systematically larger in all the models (with respect to the MODIS-DOD product) with a slight offset on the maximum value of the seasonal cycle towards spring time, particularly over Northern Sahara. It is remarkable that in these regions CNRM-3DU and NorESM show consistency in the seasonality with respect to MODIS-DOD, whereas EC-Earth and UKESM show more discrepancies on the seasonal cycle on both the amplitude and the phase. CNRM-6DU
25 model and IPSL have slight discrepancies on these 4 regions. Over Asian deserts of Taklamakan and Gobi the seasonal maximum is reasonably represented in the spring with a relative good agreement for EC-Earth, although the seasonality is not well represented for the Thar Desert. The UKESM, NorESM and CNRM-3DU models overestimate summer dust optical depth over Taklamakan desert. A common feature between all the models is that over the Asian Desert the winter values are smaller
30 than those of MODIS-DOD. Previous studies (Laurent et al., 2006) concluded that seasonal cycle of Taklamakan desert is controlled by latter spring and summer emissions which most models capture, whereas Gobi, and the associated northern China deserts, have maximum emissions during late winter and early spring. CRESCENDO ESMs reproduce the maximum values of DOD in Spring for the Gobi deserts, and UKESM and EC-Earth models capture that seasonality over Taklamakan as well.
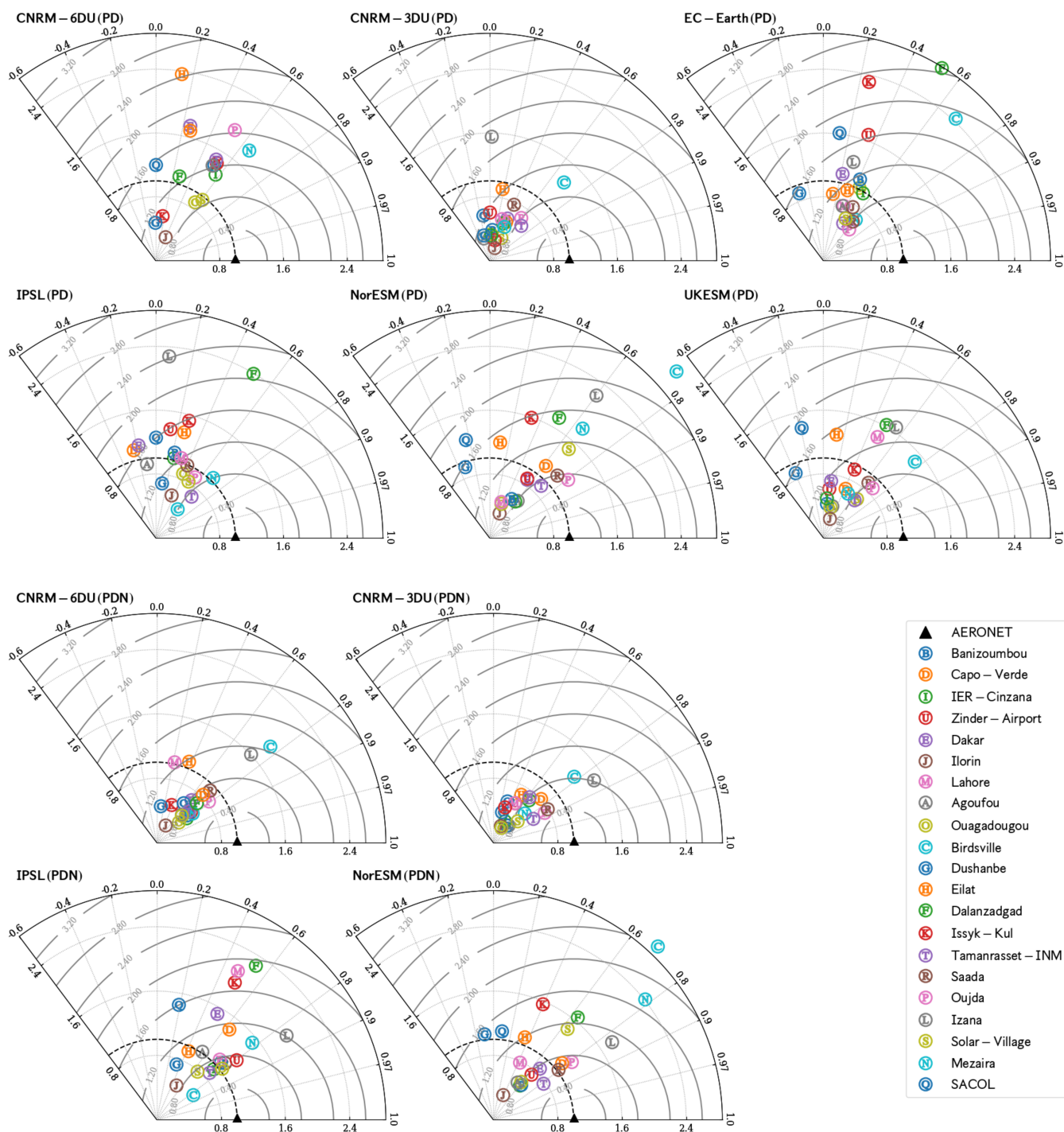
Figure 12. Normalized Taylor diagrams based for time series of total aerosol optical depths at 440nm. These diagrams are representing PD and PDN experiments and restricted to aeronet dusty stations shown in Figure 3 (with color green and blue).

Given the structural differences in the soil properties of these Asian regions (more stony at Gobi, mostly sandy at Taklamakan) and the additional role of snow cover over Gobi desert, further model studies of Asian dust emissions are needed to better constrain the way dust scheme parametrizations capture emissions in these regions. Ideally, these studies should be backed up by in-situ surface

5 concentration measurements. Regarding the Middle-East, the combined region of North and South Middle East is in agreement with Pu and Ginoux (2018b) study based on CMIP5 models.

We quantified the performance skill of the CRESCENDO ESMs by estimating the Pearson's correlation between the time-series of dust optical depth provided by each model for each of the seasons and the same time-series of dates given by the MODIS-DOD product for the period between January

10 2001 and December 2014.

Figure 11 displays the values for this Pearson's test. The overall assessment indicates marked differences between models for the same season and over the same region. In the case of the PD experiment (middle panel), the correlation between MODIS-DOD and CRESCENDO-ESM is positive over winter except in Australia and South Africa regions which are regions particularly challenging

15 for the ESMs analysed as we reported negative correlations, whereas South America is one of the regions with correlation closer to zero across all the seasons (and models). The overall correlation decreases in Spring (with respect to winter) where we notice multiple regions where the Pearson correlations are close to zero. In summer, except in the Gulf of Guinea the correlation is also smaller than in winter season. Finally, in Autumn the performance over Middle East and the Kyzyl Kum

20 region is improved. The better behaviour of all the models is given over Bodele in winter season, and the Arabian region (North and South Middle-East) that shows a reasonable agreement over all year for almost all models. Most of the features remain similar with pre-industrial aerosol-chemistry forcings (PI experiment) and the CNRM-6DU and CNMR-3DU behaves identical on PI experiment.

The agreement with satellite platforms is significantly improved for the PDN simulations and the

25 consistency between models is enhanced. In particular, the Sahara region shows a marked improvement in the simulated dust optical depth. Australia and South Africa are still the regions where the most discrepancy are found, and South America has systematically the overall values of the correlation closer to zero.

We extended the analysis based on the Pearson correlation by using the Spearman coefficient

30 which allows to detect non-linear correlations. The figure in terms of Spearman rank coefficient can be found in the supplementary information Figure S.DOD.7.

5.5.1 Network of Aerosol Optical Depth

The comparison relies on the dusty dominant AERONET stations described in section 3.4. For each station the monthly time-series of total optical depth at 440 nm are compared with the climate model
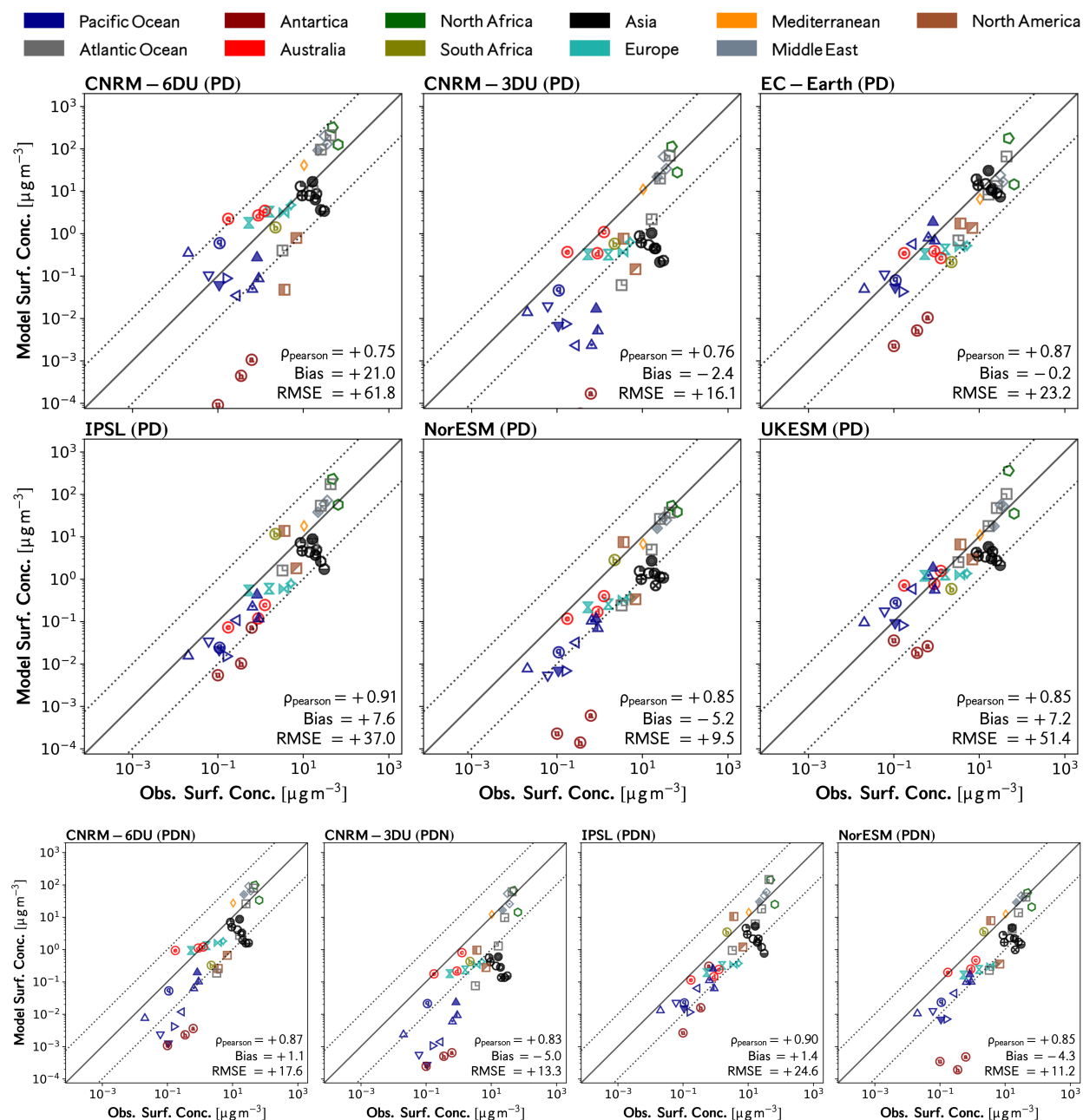
Figure 13. Comparison of dust surface concentrations in the models with the climatological dataset of (Prospero and Nees, 1986; Prospero and Savoie, 1989). The colors of the points indicate the region to which the measurement station belongs. Climatological datasets were obtained from observations over the period from 1991 to 1994. For the PI experiment see Figure S.SDC.10.

Table 12. Statistical properties of the comparision of the CRESCENDO-ESMs dust surface concentration with respect to the global network shown in Figure 2. Statistic metrics used in this table are described on Table 4. Pearson Correlation Coefficient (ρ), bias (δ), normalized bias (δ_N), Ratio standard deviations (Σ), Normalized mean absolute error (θ_N) and Root mean square error (RMSE=η).

Model	Exp.	Surface Concentration Network					
		ρ	δ	δ_N	Σ	θ_N	η
CNRM-6DU	PD	+0.76	+23.19	+1.82	+4.59	+2.26	+65.14
CNRM-3DU	PD	+0.76	-2.46	-0.19	+1.52	+0.74	+16.92
EC-Earth	PD	+0.88	-0.48	-0.04	+1.92	+0.79	+24.36
IPSL	PD	+0.91	+8.53	+0.67	+3.03	+1.26	+38.95
NorESM	PD	+0.87	-5.62	-0.44	+0.84	+0.48	+9.95
UKESM	PD	+0.84	+8.08	+0.63	+3.88	+1.30	+54.14
CNRM-6DU	PDN	+0.87	+1.33	+0.10	+1.70	+0.86	+18.59
CNRM-3DU	PDN	+0.82	-5.36	-0.42	+1.08	+0.68	+13.98
IPSL	PDN	+0.89	+1.69	+0.13	+2.15	+0.98	+25.91
NorESM	PDN	+0.86	-4.58	-0.36	+0.95	+0.55	+11.72

value of grid pixel to which the station belongs. As we are considering dusty stations, the correlation of the time-series represents how well the seasonal cycle is captured or not, while the representation of the amplitude of the cycle is measured by the standard deviation. Therefore the ratio of standard deviations is an indication of the agreement in seasonal amplitude between model and observations.

5 Those statistics are compared using the normalized Taylor diagram (Taylor, 2001). These diagrams are shown in Figure 12 for the PD and PDN simulations. The behavior of each model with respect to the observations at a station is indicated by both its radial and angle values: the radial value indicates the normalized standard deviation with respect to observations, the angle measures the correlation between time-series.

10 A common result across all models comparing the PD and PDN experiments is the higher correlation for simulations with nudged-winds, but similar normalized standard deviation for the cloud of points. With nudged winds the correlation is always positive except at one station for NorESM, a model that has correlation larger than 0.6 for 13 stations in PDN (nine stations for PD). The PD experiment has only one case with correlation values around 0.8 (NorESM at Oujda), but all the models

15 with PDN have stations with correlations larger than 0.8 indicating that the seasonal cycle of optical depth is clearly improved with wind fields from reanalysis. The CNRM-6DU model has a strong change in the normalized standard deviation from PD (for which most of the stations have values larger than 1) to PDN (with most of the stations with values smaller than 1). In terms of the amplitude of the seasonal cycle, the most challenging stations for all models are in Australia (Birdsville

20 station), Gobi Desert (Dalanzadgad and Sacol) and Izaña (close to Sahara but in an island and in

altitude). In terms of correlation Dushanbe in Thar region, and Sacol (China) are challenging. On the other side stations like Sadaa (West-Sahara), Eilat (North-Middle-East) or Dakar are reasonably well captured by models.

5.6 Surface Concentrations

5   The stations were chosen to cover a range of dust values from low to moderate dust concentrations, mainly located at a distance from the main dust emission regions. According to the instrument location, Sahel and the West coast of North Africa (green and grey squared) together with middle east stations (grey diamonds) report the highest values of surface concentrations. The group represented by black circles represents moderate values indicating transport of dust from arid and semi-arid re-

10 gions of East Asia. The lowest values correspond at Antarctica and the Pacific Ocean (blue triangles).

    The comparison between the CRESCENDO models and a network of stations that measure dust surface concentrations is shown in Figure 13 for PD experiment and in Figure S.DD.1 of the supplement for the nudged-wind simulations (Figure S.DD.2 shows the PI results). The agreement falls into the same range than previous comparisons with CAM model (Albani et al., 2014) where the full

15 range for the expected differences in annual mean values is close to 10. This range of differences between models compares well with the previous study from Huneeus et al. (2011)

    CNRM-3DU underestimates dust concentrations over the Pacific Ocean. This behavior over regions remote from dust sources could be partly due to the non-conservative semi-Lagrangian transport scheme that accentuates the differences with the distance of transport (a fact also consistent

20 with their values of the Pearson correlation, mainly in nudged-simulations). All models except IPSL underestimate the concentrations in the Antarctica station. This could be due to the larger emissions from Patagonia that cause the increase in correlation coefficient for this model. Over Northern Europe all models, except CNRM, tend to underestimate dust concentrations and do not reproduce the range of variability found in the observations. When comparing PD and PDN simulations, IPSL and

25 NorESM models show slightly better agreement in PDN conditions, whereas the two CNRM models show higher correlations when using nudged-winds but similar differences over the Pacific Ocean.

    The correlation between model and observations is significant for all models. The RMSE values are influenced by the stations with the highest concentrations and hence are more representative of the concentrations near the Sahara desert and the Middle East. In this regard, NorESM and CNRM-

30 3DU models show the best agreement over these regions. The EC-Earth model shows however the smallest bias because it better captures dust concentrations over Japan and East China, where all other models underestimate concentrations. Values of normalized bias and normalized mean absolute error complement the previous metrics give us a characterization of global differences account-
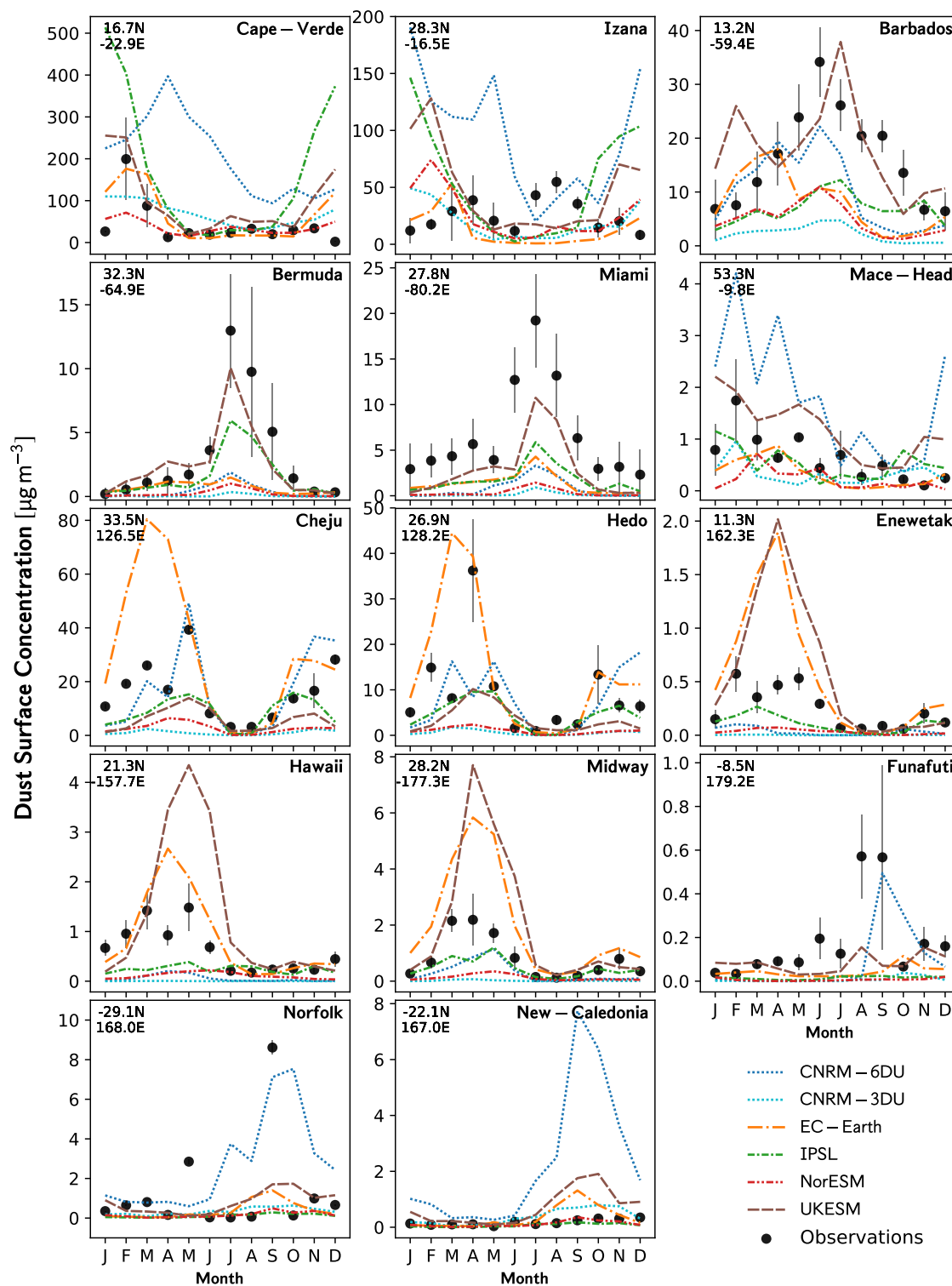
Figure 14. Comparison of ESM models (PD) of dust surface concentration with a station based climatological dataset. For PI and PDN experiment see the supplement figures S.DSC.7 and S.DSC.8.

ing equally for the stations with the lowest concentrations (see Table 12), the normalized statistics indicate that the nudged-wind simulations generally show a better agreement with observations.

Although the 36 stations are covering many regions, a complete assessment of the model performance at the surface is not possible due to the absence of stations in South America and Asia,
5 and only one station inland over North America and Africa. Therefore, the global observational constrains in terms of surface concentrations is only partial.

The comparison of the seasonal cycle of surface concentrations against 14 stations is shown in Figure 14 for PD experiment. The stations Cape-Verde and Barbados are in the same latitude at opposite sides of the Atlantic therefore they have a signature of the transatlantic transport of min-
10 eral dust from Sahel region. IPSL, CNRM-6DU and UKESM models overestimate the early winter contributions to the seasonal cycle in Cape-Verde. The models reproduce the concentrations within a factor two from May to September (except CNRM-6DU model) in general with an overestimation except for EC-Earth. However in the case of Barbados UKESM after April and CNRM-6DU before May reproduce very well the surface concentrations. All the other models although with a
15 similar seasonal cycle underestimate the total surface concentrations by a factor from 2 to 4. The stations Izaña, Bermudas, Miami have also similar latitudes and represent the Atlantic transport from West-Sahara. Izaña Observatory is not a sea level and all the models have difficulties to reproduce the seasonal cycle. The seasonal cycles of Bermuda and Miami are well reproduced with withj a general understimation of the surface cocentrations values, where only UKESM and IPSL
20 show a consistency within a factor 2. Cheju and Hedo are stations on the Eastern Pacific Coast and their measurements are representing the dust transport from China. EC-Earth reproduces well the seasonal cycle but with an overestimation of spring concentrations by a factor 3. The seasonal cycle and values are well represented by CNRM-6DU and IPSL model. Enewetak is located between Filipinas and Hawai in the middle of Pacific Ocean, EC-Earth and UKESM overestimate the spring
25 concentrations whereas all the other models understimate them. A similar sitation is found in Hawai and Midway. The rest of the stations are in the Southern Hemisphere where the dust concentrations are smaller and the seasonal cycle is only partially reproduced. The results for the PDN experiment (see supplement DSC) are similar with a slight improvement in the seasonal cycle but with a general underestimation of surface concentrations. All the models with nudged winds exhibit problems in
30 reproducing the observations in Izaña.

6 Discussion

The analysis of the results provides insight on how both modelling and measuring dust can be used to improve our understanding of the dust cycle. More specifically, through comparison of emission

and total deposition fluxes we are able to propose specific areas for which improvements are needed. Annual global dust emissions are dependent on the dust particle size distribution (DPSD) representation and models that account for particles with diameters larger than 10 μm produce higher total fluxes. To overcome the challenge of comparing models with different DPSD, we introduced
5   normalized emission maps, showing first by a comparison between PD and PDN simulations that wind fields do not affect substantially these normalized emission estimates. This led us to interpret differences in regions where dust was emitted as reflecting differences in underlying *effective* soil erodibility information among models (including soil moisture effects)

    With the aim to reproduce dust observations at different model resolutions, models have intro-
10 duced correction factors to those soil erodibility (see for example (Albani et al., 2014; Knippertz and Todd, 2012)). But our normalized emissions indicate effective model differences, both in intensity and location, on preferential dust sources. Those differences are the largest over Asia and are also significant over Australia. Hence we identified these regions as two source regions that would benefit from further comparison of dust emission observations with actual model occurrences in emission
15 fluxes. Additional research is also needed to ascertain seasonality disagreements in dust sources.

    The model ensemble values of total emissions with nudged winds has less dispersion. We stress however that dust column loads are a better quantity when comparing models with different size distribution at emission than compare to total emission fluxes, since gravitational settling gets rid of the very large particles over a short time span. For dust loads, all models are in a range between
20 9.1 and 15.2 [Tg/yr] which can serve as a baseline to study model improvements. Another important point of discrepancy between models is the ratio between wet and dry deposition over similar particle size range, indicating that specific sensitivity studies should focus on the treatment of deposition. We also evidenced significant differences in deposition over oceans, in particular over the Indian Ocean and over the Pacific East, both of which are affected by dust source distributions over Asia.

25   Regarding the direct radiative effects, it is important to ascertain an uncertainty range for each model. Based on a calculation with 4 modes over a range from 0.1 to 100 μm, we observe that those models without the smallest particles (without mode m_1) will underestimate the short-wave contribution at TOA by up to 20%. Models without the largest particles (those represented by the m_{ww}, ie. for bins with radius larger than 40μm) are expected however to not be significantly affected
30 in their estimations of DRE in the SW.

    Because the dust emissions depend on mineralogy, on land surface properties and on regional meteorology, a few in-situ measurements are not sufficient to constrain the dust cycle at any scale. It appeared logical to try to constrain the dust cycle by relying on dust optical depth (DOD) estimated from the satellite observations. (Ridley et al., 2016) used retrievals from instruments on-
35 board MODIS and MISR to estimate global values for DOD between 0.020 and 0.035 which place

two models (CNRM-C6 and UKESM) outside this observational range. Although DOD should be proportional to the mineral dust total column, models with the lowest dust loadings are not those with smaller DOD. This is illustrated in the differences on mass extinction efficiency between the different models. The magnitude of this property is a good indicator of intrinsic model properties due to its relatively small seasonal cycle. Mass extinction efficiency is affected by the DPSD and optical properties of mineral dust modelled. Note however that there are a sensible difficulty in estimate DAOD from satellite retrievals with the method of (Ridley et al., 2016) because it still lies on model simulations to ascertain the fraction of non-dust optical depths. As shown by our results in supplement material (section DOD), the non-dust fraction of optical depths can have large inter-model differences.

Therefore, based on MODIS satellite estimations of DOD based upon algorithm described in (Pu and Ginoux, 2018b), we compared the regional dust optical depth over dust source regions. This comparison allowed us to evaluate the skill of each model by evaluating the correlation between the regional time series of observations versus each model. A significant increase in the skill was revealed for the simulations using nudged winds, indicating that a consistent reproduction of the seasonal cycle depends critically on how the strong surface winds are represented. This part of the wind distribution being more consistent when using winds from the ERA-Interim re-analysis. The correlation is not informing on differences in the scale of the signal, and Figure DOD.3 shows that there are regions where the seasonal cycle is well reproduced but the mean annual signal is actually underestimated, see also (Pu and Ginoux, 2018b).

7 Conclusions

This paper analyses the representation of the mineral dust cycle in five ESMs through diagnostics used for the evaluation of their performance with regards to observations. Although the agreement in terms of aerosol optical depth is better than surface fluxes or concentrations, we separate the models into two groups based on the simulated global mean dust optical depth. Those models with values closer to 0.025 (CNRM, EC-Earth, IPSL and UKESM) are more consistent with the proposed satellite estimations (Ridley et al., 2016). Given that the optical depths depends on column loadings rather than dust emission fluxes, the inter-model convergence can be achieved even for those models that are not implementing particles with radius larger than 10μm. Also, to achieve an inter-model convergence in terms of optical depths is important to better constrain the dust radiative forcings and direct radiative effects (DRE). Note that according to (Biagio et al., 2020) and to our results of Table 6 the DRE at the top of the atmosphere and at the surface have an important contribution from particles with diameters larger than 10μm altough the contribution of the fraction of particles larger

than 40μm is marginal. The DOD seasonal cycle asserted by MODIS satellite estimates (see (Pu and Ginoux, 2018b)) gives us a key reference to understand the sources of the model discrepancies as illustrated by figure 11. The second diagnostic that we find useful is the mass extinction efficency (MEE) coefficient has a smaller inter-annual variability are reflects modelling properties such as

5   assumptions on the size distribution modelled.

The models exhibit important differences in preferential dust sources, in particular a better agreement of preferential sources found over Asia and Australia would give us more consistency on global dust transport over the Indian and the Pacific Oceans. Although there is an scarcity of measurement campaigns over Asia compared to the Sahara and Sahel, studies based on empirical relationships

10   between visibility and dust surface concentrations give us an additional insight on dust sources over these regions (Shao and Dong, 2006). Compared to (Huneeus et al., 2011) we added AERONET stations over Asia, which resulted to be challenging for the CRESCENDO-ESMs in terms of the comparison provided by Taylor diagrams (see figure 12).

Currently, the dust source disagreements/differences between models make it difficult to quantify

15   the fraction of the uncertainties of dust emission due to those small-scale atmospheric phenomena not well represented by global models. The use of wind fields from reanalysis datasets reduces the differences between models, but a benchmark reference dataset regarding dust sources is needed to establish a range for those uncertainties.

Note also that the global description of dust cycle in terms of the amount of aerosol mass mobilized

20   needs to be extended to larger particles as they can significantly increase the total emissions, and according to recent studies the fraction of dust mass in the atmosphere due to the coarser particles would be dominant with respect to fine mode (Adebiyi and Kok, 2020). However, still the method in which they are incorporated in the models can drive strong differences in total emissions with ranges from 3500 $\mathrm{Tg\,yr^{-1}}$ of CNRM-6DU to 7000 $\mathrm{Tg\,yr^{-1}}$ of UKESM model. Even more these

25   differences in total emissions are not directly translated in proportional loadings because of the differences in deposition between models and therefore in the lifetime.

Regarding total deposition one priority should be given to analyze the large differences in the ratio between dry and wet deposition between models and observations which is only partially explained by the modelled size distribution. From the aerosol micro-physical point of view differences

30   in the dominance of wet scavenging over ocean regions could account for part of these differences. Whereas, as indicated by (Shao et al., 2011) observations of dry deposition velocities in wind tunnels are not reproduced by current dry deposition schemes. At present, all models have difficulties to estimate local values wet/dry depositions, which can exceed a factor of 10.

Appendix A: Methods to estimate Direct Radiative Effects in multi-modal size distributions

In section 5.1 it was shown the direct radiative effects for a dust scheme with several dust modes. Here we present the methods used to obtain the results of Table 6. The *direct radiative effect* is defined by the *earth instantaneous imbalance* at the top of the atmosphere due to a specific at-
5 mospheric specie/component introduced at (Boucher and Tanré, 2000) and discussed by Bellouin et al. (2013); Heald et al. (2014). This imbalance is conceptually different from the radiative forcing (either defined as an stratospherically adjusted instantaneous radiative forcing or by an effective radiative forcing) which is a comparison between a pre-industrial and a present day. In our case the estimations of direct radiative effects are estimated during a single simulation with present day con-
10 ditions but with multiple calls to the radiative transfer model implemented in the climate model. The aerosols in the climate model have actually direct, indirect and semi-direct effects along the simulation but the method only estimated the direct radiative effects due to scattering and absorption of specific aerosol species. Therefore there are observational based estimations of the direct radiative effects of the aerosols (Yu et al., 2006). However, from the point of view of aerosol modeling based
15 on multi-modal approaches it has been reported a non-linearity properties for the estimation of each mode contribution (Biagio et al., 2020) here the two different approaches and a joint new method with four calls to the radiative scheme are described.

In general, in the calculation done by current radiative transfer schemes it is considered a state of the atmosphere with several aerosols species $\mathcal{X}, \mathcal{Y}, \ldots$ where each specie is possibly described by
20 a multi-modal distribution with modes $X_1, \ldots, X_n$. The state with all the aerosol species is named hereafter $\mathcal{A}$, therefore $\mathcal{A} = \mathcal{X} \cup \mathcal{Y} \cup \mathcal{Z} \cup \ldots$. We define another state named $\widetilde{\mathcal{A}}$ that includes all the modes of every aerosol specie except those modes corresponding of the specie $\mathcal{X}$. Therefore, $\mathcal{A} = \widetilde{\mathcal{A}} \cup \mathcal{X}$. The radiative effect of the aerosol $\mathcal{X}$ described by several modes $X_1, \ldots, X_n$, would be,

$$\widehat{\mathcal{F}_X} = \mathcal{R}(\mathcal{A}, \delta) - \mathcal{R}(\widetilde{\mathcal{A}}, \delta)$$

25 where $\mathcal{R}$ represents the radiance obtained in our radiative transfer scheme which is intrinsically a non-linear forward model. δ represents all others elements considered by our radiative scheme beyond the aerosol species which are invariant for both estimation of the radiance.

However, in order to disentangle the contribution of each mode X_i of the specie $\mathcal{X}$, there results differs depending on the methodology used due to the non linearity of $\mathcal{R}$. We define here two
30 methods: the first approach considers each X_i mode added individually to $\widetilde{\mathcal{A}}$ with respect to the experiment given by $\widetilde{\mathcal{A}}$, hereafter we name this as *method in*. The second approach compares a experiment $\mathcal{A}$ with a scenario $\widetilde{\mathcal{A}}$ where all the modes X_j with $j \neq i$ are included, named hereafter *method out*.

The method A would be written for the radiative effects of X_i as,

$$\widehat{\mathcal{F}_{X_i}} = \mathcal{R}(\widetilde{\mathcal{A}} \cup X_i, \delta) - \mathcal{R}(\widetilde{\mathcal{A}}, \delta)$$

whereas the method B is written as,

$$\mathcal{F}_{X_i} = \mathcal{R}(\mathcal{A}, \delta) - \mathcal{R}(\mathcal{A} \cup X_i^*, \delta) \quad \text{with} \quad X_i^* = \cup_{i \neq j} X_j$$

5   we note that $\mathcal{F}_X = \widehat{\mathcal{F}_X}$ but $\mathcal{F}_{X_i} \neq \widehat{\mathcal{F}_{X_i}}$. In particular, we have both, $\sum_i \mathcal{F}_{X_i} \neq \mathcal{F}_X$ and $\sum_i \widehat{\mathcal{F}_{X_i}} \neq \widehat{\mathcal{F}_X}$. However, the results for 4 modes of mineral dust of IPSL showed at Table 6 indicate that $\frac{1}{2}\sum_i (\widehat{\mathcal{F}_{X_i}} + \mathcal{F}_{X_i}) \approx \widehat{\mathcal{F}_X} = \mathcal{F}_X$.

Therefore the joint method based on four calls to the radiative scheme to calculate the direct radiative effect is providing estimations per mode that combine linearly to reproduce the multimodal
10 direct radiative effect.

Code availability.   The core functions of the software used for data-analysis is available on the reference (Checa-Garcia, 2020)

Author contributions.   R.CG and YB designed the research. R.CG analysed the data and wrote the manuscript with input from YB, SA, PN, DO, AC and TvN. Data from climate model simulations were provided by: TB,
15 P.LS and TvN for EC-Earth, MS and DO for NorESM, FO and CD for the UKESM, MM and PN for the CNRM, R.CG for IPSL and IPSL-4DU. SA, YB and AC developed the IPSL-4DU dust scheme. BM and J.MP provided observational datasets used in the analysis.

Competing interests.   The authors declare that they have no conflict of interest.

Acknowledgements.   This work has been supported by the European Union's Horizon 2020 research and inno-
20 vation programme under grant agreement No 641816 (CRESCENDO). S.A. acknowledges funding from the European Union's Horizon 2020 research and innovation program under the Marie Sklodowska-Curie grant agreement 708119, for the project DUS3C. The French National Observatory Service INDAAF is supported by the INSU/CNRS, the IRD(Institut de Recherche pour le Développement) and the Observatoires des Sciences de l'Univers EFLUVE and Observatoire Midi-Pyrénées. The authors would like to thank the French and African

PIs and operators for maintaining the stations and providing the PM10 concentrations. The INDAAF data are distributed on the web site : https://indaaf.obs-mip.fr/. We thank to Mohit Dalvi for their support with UKESM, and Jane Mulcahy for implement the AMIP in the UKESM.

References

Adebiyi, A. A. and Kok, J. F.: Climate models miss most of the coarse dust in the atmosphere, Science Advances, 6, eaaz9507, https://doi.org/10.1126/sciadv.aaz9507, https://doi.org/10.1126/sciadv.aaz9507, 2020.

Adebiyi, A. A., Kok, J. F., Wang, Y., Ito, A., Ridley, D. A., Nabat, P., and Zhao, C.: Dust Constraints from joint
5   Observational-Modelling-experiMental analysis (DustCOMM): comparison with measurements and model simulations, Atmospheric Chemistry and Physics, 20, 829–863, https://doi.org/10.5194/acp-20-829-2020, https://doi.org/10.5194/acp-20-829-2020, 2020.

Albani, S. and et al: The global dust cycle in the IPSL climate model revisited: particle size distributions and dependence of emissions on land surface properties, in preparation, 2020.

10 Albani, S., Mahowald, N. M., Perry, A. T., Scanza, R. A., Zender, C. S., Heavens, N. G., Maggi, V., Kok, J. F., and Otto-Bliesner, B. L.: Improved dust representation in the Community Atmosphere Model, Journal of Advances in Modeling Earth Systems, 6, 541–570, https://doi.org/https://doi.org/10.1002/2013MS000279, 2014.

Alfaro, S. C. and Gomes, L.: Modeling mineral aerosol production by wind erosion: Emission intensi-
15 ties and aerosol size distributions in source areas, Journal of Geophysical Research: Atmospheres, 106, 18 075–18 084, https://doi.org/10.1029/2000JD900339, https://agupubs.onlinelibrary.wiley.com/doi/abs/10.1029/2000JD900339, 2001.

Alfaro, S. C., Gaudichet, A., Gomes, L., and Maillé, M.: Modeling the size distribution of a soil aerosol produced by sandblasting, Journal of Geophysical Research: Atmospheres, 102, 11 239–11 249,
20 https://doi.org/10.1029/97JD00403, https://agupubs.onlinelibrary.wiley.com/doi/abs/10.1029/97JD00403, 1997.

Alfaro, S. C., Gaudichet, A., Gomes, L., and Maillé, M.: Mineral aerosol production by wind erosion: Aerosol particle sizes and binding energies, Geophysical Research Letters, 25, 991–994, https://doi.org/10.1029/98GL00502, https://agupubs.onlinelibrary.wiley.com/doi/abs/10.1029/98GL00502,
25 1998.

Allen, C. J. T., Washington, R., and Saci, A.: Dust detection from ground-based observations in the summer global dust maximum: Results from Fennec 2011 and 2012 and implications for modeling and field observations, Journal of Geophysical Research: Atmospheres, 120, 897–916, https://doi.org/10.1002/2014jd022655, https://doi.org/10.1002%2F2014jd022655, 2015.

30 Astitha, M., Lelieveld, J., Abdel Kader, M., Pozzer, A., and de Meij, A.: New parameterization of dust emissions in the global atmospheric chemistry-climate model EMAC, Atmospheric Chemistry & Physics Discussions, 12, 13 237–13 298, https://doi.org/https://doi.org/10.5194/acpd-12-13237-2012, http://adsabs.harvard.edu/abs/2012ACPD...1213237A, 2012.

Atkinson, J., Murray, B., Woodhouse, M., Whale, T., Baustian, K., Carslaw, K., Dobbie, S., O'Sullivan, D., and
35 Malkin, T.: The importance of feldspar for ice nucleation by mineral dust in mixed-phase clouds, Nature, 498, https://doi.org/10.1038/nature12278, 2013.

Bauer, S. E.: Global modeling of heterogeneous chemistry on mineral aerosol surfaces: Influence on tropospheric ozone chemistry and comparison to observations, Journal of Geophysical Research, 109, https://doi.org/10.1029/2003jd003868, https://doi.org/10.1029/2003jd003868, 2004.

Bègue, N., Tulet, P., Pelon, J., Aouizerats, B., Berger, A., and Schwarzenboeck, A.: Aerosol processing and CCN formation of an intense Saharan dust plume during the EUCAARI 2008 campaign, Atmospheric Chemistry and Physics, 15, 3497–3516, https://doi.org/10.5194/acp-15-3497-2015, https://acp.copernicus.org/articles/15/3497/2015/, 2015.

Bellouin, N., Boucher, O., Haywood, J., and Reddy, M. S.: Global estimate of aerosol direct radiative forcing from satellite measurements, Nature, 438, 1138–1141, https://doi.org/10.1038/nature04348, https://doi.org/10.1038%2Fnature04348, 2005.

Bellouin, N., Quaas, J., Morcrette, J.-J., and Boucher, O.: Estimates of aerosol radiative forcing from the MACC re-analysis, Atmospheric Chemistry and Physics, 13, 2045–2062, https://doi.org/10.5194/acp-13-2045-2013, https://doi.org/10.5194/acp-13-2045-2013, 2013.

Biagio, C. D., Balkanski, Y., Albani, S., Boucher, O., and Formenti, P.: Direct Radiative Effect by Mineral Dust Aerosols Constrained by New Microphysical and Spectral Optical Data, Geophysical Research Letters, 47, https://doi.org/10.1029/2019gl086186, https://doi.org/10.1029/2019gl086186, 2020.

Biasutti, M.: Rainfall trends in the African Sahel: Characteristics, processes, and causes, Wiley Interdisciplinary Reviews: Climate Change, 10, e591, https://doi.org/10.1002/wcc.591, https://onlinelibrary.wiley.com/doi/abs/10.1002/wcc.591, 2019.

Boucher, O. and Tanré, D.: Estimation of the aerosol perturbation to the Earth's Radiative Budget over oceans using POLDER satellite aerosol retrievals, Geophysical Research Letters, 27, 1103–1106, https://doi.org/10.1029/1999GL010963, https://agupubs.onlinelibrary.wiley.com/doi/abs/10.1029/1999GL010963, 2000.

Boucher, O., Servonnat, J., Albright, A. L., Aumont, O., Balkanski, Y., Bastrikov, V., Bekki, S., Bonnet, R., Bony, S., Bopp, L., Braconnot, P., Brockmann, P., Cadule, P., Caubel, A., Cheruy, F., Codron, F., Cozic, A., Cugnet, D., D'Andrea, F., Davini, P., de Lavergne, C., Denvil, S., Deshayes, J., Devilliers, M., Ducharne, A., Dufresne, J.-L., Dupont, E., Éthé, C., Fairhead, L., Falletti, L., Flavoni, S., Foujols, M.-A., Gardoll, S., Gastineau, G., Ghattas, J., Grandpeix, J.-Y., Guenet, B., Guez, Lionel, E., Guilyardi, E., Guimberteau, M., Hauglustaine, D., Hourdin, F., Idelkadi, A., Joussaume, S., Kageyama, M., Khodri, M., Krinner, G., Lebas, N., Levavasseur, G., Lévy, C., Li, L., Lott, F., Lurton, T., Luyssaert, S., Madec, G., Madeleine, J.-B., Maignan, F., Marchand, M., Marti, O., Mellul, L., Meurdesoif, Y., Mignot, J., Musat, I., Ottlé, C., Peylin, P., Planton, Y., Polcher, J., Rio, C., Rochetin, N., Rousset, C., Sepulchre, P., Sima, A., Swingedouw, D., Thiéblemont, R., Traore, A. K., Vancoppenolle, M., Vial, J., Vialard, J., Viovy, N., and Vuichard, N.: Presentation and Evaluation of the IPSL-CM6A-LR Climate Model, Journal of Advances in Modeling Earth Systems, 12, e2019MS002 010, https://doi.org/10.1029/2019MS002010, https://agupubs.onlinelibrary.wiley.com/doi/abs/10.1029/2019MS002010, e2019MS002010 10.1029/2019MS002010, 2020.

Checa-Garcia, R.: CMIP6 Ozone forcing dataset: supporting information, https://doi.org/10.5281/zenodo.1135127, https://doi.org/10.5281/zenodo.1135127, 2018.

Checa-Garcia, R.: FunFAN: FUNctions For Aerosol Modelling (v1.0), Zenodo (10.5281/zenodo.3672001), https://doi.org/10.5281/zenodo.3672001, https://doi.org/10.5281/zenodo.3672001, 2020.

Checa-Garcia, R., Hegglin, M. I., Kinnison, D., Plummer, D. A., and Shine, K. P.: Historical Tropospheric and Stratospheric Ozone Radiative Forcing Using the CMIP6 Database, Geophysical Research Letters, 45, 3264–3273, https://doi.org/10.1002/2017GL076770, https://agupubs.onlinelibrary.wiley.com/doi/abs/10.1002/2017GL076770, 2018.

Colarco, P. R., Nowottnick, E. P., Randles, C. A., Yi, B., Yang, P., Kim, K.-M., Smith, J. A., and Bardeen, C. G.: Impact of radiatively interactive dust aerosols in the NASA GEOS-5 climate model: Sensitivity to dust particle shape and refractive index, Journal of Geophysical Research (Atmospheres), 119, 753–786, https://doi.org/https://doi.org/10.1002/2013JD020046, http://adsabs.harvard.edu/abs/2014JGRD..119..753C, 2014.

Denjean, C., Cassola, F., Mazzino, A., Triquet, S., Chevaillier, S., Grand, N., Bourrianne, T., Momboisse, G., Sellegri, K., Schwarzenbock, A., Freney, E., Mallet, M., and Formenti, P.: Size distribution and optical properties of mineral dust aerosols transported in the western Mediterranean, Atmospheric Chemistry and Physics, 16, 1081–1104, https://doi.org/10.5194/acp-16-1081-2016, https://www.atmos-chem-phys.net/16/1081/2016/, 2016.

Dentener, F. J., Carmichael, G. R., Zhang, Y., Lelieveld, J., and Crutzen, P. J.: Role of mineral aerosol as a reactive surface in the global troposphere, Journal of Geophysical Research: Atmospheres, 101, 22 869–22 889, https://doi.org/10.1029/96JD01818, https://agupubs.onlinelibrary.wiley.com/doi/abs/10.1029/96JD01818, 1996.

Diner, D. J., Beckert, J. C., Bothwell, G. W., and Rodriguez, J. I.: Performance of the MISR instrument during its first 20 months in Earth orbit, IEEE Transactions on Geoscience and Remote Sensing, 40, 1449–1466, https://doi.org/10.1109/tgrs.2002.801584, https://doi.org/10.1109/Ftgrs.2002.801584, 2002.

Evan, A. T., Fiedler, S., Zhao, C., Menut, L., Schepanski, K., mant, C. F., and Doherty, O.: Derivation of an observation-based map of North African dust emission, Aeolian Research, 16, 153 – 162, https://doi.org/https://doi.org/10.1016/j.aeolia.2015.01.001, http://www.sciencedirect.com/science/article/pii/S187596371500004X, 2015.

Giles, D. M., Sinyuk, A., Sorokin, M. G., Schafer, J. S., Smirnov, A., Slutsker, I., Eck, T. F., Holben, B. N., Lewis, J. R., Campbell, J. R., Welton, E. J., Korkin, S. V., and Lyapustin, A. I.: Advancements in the Aerosol Robotic Network (AERONET) Version 3 database – automated near-real-time quality control algorithm with improved cloud screening for Sun photometer aerosol optical depth (AOD) measurements, Atmospheric Measurement Techniques, 12, 169–209, https://doi.org/10.5194/amt-12-169-2019, https://www.atmos-meas-tech.net/12/169/2019/, 2019.

Ginoux, P.: Warming or cooling dust?, Nature Geoscience, 10, 246–248, https://doi.org/10.1038/ngeo2923, https://doi.org/10.1038%2Fngeo2923, 2017.

Ginoux, P., Chin, M., Tegen, I., Prospero, J. M., Holben, B., Dubovik, O., and Lin, S.-J.: Sources and distributions of dust aerosols simulated with the GOCART model, Journal of Geophysical Research: At-

mospheres, 106, 20 255–20 273, https://doi.org/10.1029/2000JD000053, https://agupubs.onlinelibrary.wiley.com/doi/abs/10.1029/2000JD000053, 2001.

Gläser, G., Kerkweg, A., and Wernli, H.: The Mineral Dust Cycle in EMAC 2.40: sensitivity to the spectral resolution and the dust emission scheme, Atmospheric Chemistry & Physics, 12, 1611–1627, https://doi.org/https://doi.org/10.5194/acp-12-1611-2012, http://adsabs.harvard.edu/abs/2012ACP....12.1611G, 2012.

Gruber, N., Gloor, M., Mikaloff Fletcher, S. E., Doney, S. C., Dutkiewicz, S., Follows, M. J., Gerber, M., Jacobson, A. R., Joos, F., Lindsay, K., Menemenlis, D., Mouchet, A., Müller, S. A., Sarmiento, J. L., and Takahashi, T.: Oceanic sources, sinks, and transport of atmospheric $CO2$, Global Biogeochemical Cycles, 23, https://doi.org/10.1029/2008GB003349, https://agupubs.onlinelibrary.wiley.com/doi/abs/10.1029/2008GB003349, 2009.

Heald, C. L., Ridley, D. A., Kroll, J. H., Barrett, S. R. H., Cady-Pereira, K. E., Alvarado, M. J., and Holmes, C. D.: Contrasting the direct radiative effect and direct radiative forcing of aerosols, Atmospheric Chemistry and Physics, 14, 5513–5527, https://doi.org/10.5194/acp-14-5513-2014, https://acp.copernicus.org/articles/14/5513/2014/, 2014.

Heinold, B., Knippertz, P., Marsham, J. H., Fiedler, S., Dixon, N. S., Schepanski, K., Laurent, B., and Tegen, I.: The role of deep convection and nocturnal low-level jets for dust emission in summertime West Africa: Estimates from convection-permitting simulations, Journal of Geophysical Research: Atmospheres, 118, 4385–4400, https://doi.org/10.1002/jgrd.50402, https://agupubs.onlinelibrary.wiley.com/doi/abs/10.1002/jgrd.50402, 2013.

Hoose, C. and Möhler, O.: Heterogeneous ice nucleation on atmospheric aerosols: a review of results from laboratory experiments, Atmospheric Chemistry & Physics, 12, 9817–9854, https://doi.org/10.5194/acp-12-9817-2012, http://adsabs.harvard.edu/abs/2012ACP....12.9817H, 2012.

Huneeus, N., Schulz, M., Balkanski, Y., Griesfeller, J., Prospero, J., Kinne, S., Bauer, S., Boucher, O., Chin, M., Dentener, F., Diehl, T., Easter, R., Fillmore, D., Ghan, S., Ginoux, P., Grini, A., Horowitz, L., Koch, D., Krol, M. C., Landing, W., Liu, X., Mahowald, N., Miller, R., Morcrette, J.-J., Myhre, G., Penner, J., Perlwitz, J., Stier, P., Takemura, T., and Zender, C. S.: Global dust model intercomparison in AeroCom phase I, Atmospheric Chemistry and Physics, 11, 7781–7816, https://doi.org/10.5194/acp-11-7781-2011, https://www.atmos-chem-phys.net/11/7781/2011/, 2011.

Kaufman, Y. J., Koren, I., Remer, L. A., Tanré, D., Ginoux, P., and Fan, S.: Dust transport and deposition observed from the Terra-Moderate Resolution Imaging Spectroradiometer (MODIS) spacecraft over the Atlantic Ocean, Journal of Geophysical Research: Atmospheres, 110, https://doi.org/10.1029/2003JD004436, https://agupubs.onlinelibrary.wiley.com/doi/abs/10.1029/2003JD004436, 2005.

Kirkevåg, A., Grini, A., Olivié, D., Seland, Ø., Alterskjær, K., Hummel, M., Karset, I. H. H., Lewinschal, A., Liu, X., Makkonen, R., Bethke, I., Griesfeller, J., Schulz, M., and Iversen, T.: A production-tagged aerosol module for Earth system models, OsloAero5.3 – extensions and updates for CAM5.3-Oslo, Geoscientific Model Development, 11, 3945–3982, https://doi.org/10.5194/gmd-11-3945-2018, https://www.geosci-model-dev.net/11/3945/2018/, 2018.

Klingmüller, K., Metzger, S., Abdelkader, M., Karydis, V. A., Stenchikov, G. L., Pozzer, A., and Lelieveld, J.: Revised mineral dust emissions in the atmospheric chemistry–climate model EMAC (MESSy 2.52 DU-Astitha1 KKDU2017 patch), Geoscientific Model Development, 11, 989–1008, https://doi.org/10.5194/gmd-11-989-2018, https://doi.org/10.5194%2Fgmd-11-989-2018, 2018.

5 Knippertz, P. and Stuut, J.-B. W., eds.: Mineral Dust - A Key Player in the Earth System, Springer-Verlag, https://doi.org/10.1007/978-94-017-8978-3, 2014.

Knippertz, P. and Todd, M. C.: Mineral dust aerosols over the Sahara: Meteorological controls on emission and transport and implications for modeling, Reviews of Geophysics, 50, https://doi.org/10.1029/2011RG000362, https://agupubs.onlinelibrary.wiley.com/doi/abs/10.1029/ 10 2011RG000362, 2012.

Kohfeld, K. and Harrison, S.: DIRTMAP: The geological record of dust, Earth-Science Reviews, 54, 81 – 114, 2001.

Kok, J. F.: A scaling theory for the size distribution of emitted dust aerosols suggests climate models underestimate the size of the global dust cycle, Proceedings of the National Academy of Sciences, 108, 1016–1021, 15 https://doi.org/10.1073/pnas.1014798108, https://www.pnas.org/content/108/3/1016, 2011.

Kok, J. F., Ridley, D. A., Zhou, Q., Miller, R. L., Zhao, C., Heald, C. L., Ward, D. S., Albani, S., and Haustein, K.: Smaller desert dust cooling effect estimated from analysis of dust size and abundance, Nature Geoscience, 10, 274–, https://doi.org/10.1038/ngeo2912, 2017.

Konare, A., Zakey, A. S., Solmon, F., Giorgi, F., Rauscher, S., Ibrah, S., and Bi, X.: A regional climate modeling study of the effect of desert dust on the West African monsoon, Journal of Geophysical Research: 20 Atmospheres, 113, https://doi.org/10.1029/2007JD009322, https://agupubs.onlinelibrary.wiley.com/doi/abs/ 10.1029/2007JD009322, 2008.

Laurent, B., Marticorena, B., Bergametti, G., and Mei, F.: Modeling mineral dust emissions from Chinese and Mongolian deserts, Global and Planetary Change, 52, 121 – 141, 25 https://doi.org/https://doi.org/10.1016/j.gloplacha.2006.02.012, http://www.sciencedirect.com/science/ article/pii/S0921818106000348, monitoring and Modelling of Asian Dust Storms, 2006.

LeGrand, S. L., Polashenski, C., Letcher, T. W., Creighton, G. A., Peckham, S. E., and Cetola, J. D.: The AFWA dust emission scheme for the GOCART aerosol model in WRF-Chem v3.8.1, Geoscientific Model Development, 12, 131–166, https://doi.org/10.5194/gmd-12-131-2019, https://doi.org/10.5194% 30 2Fgmd-12-131-2019, 2019.

Li, F., Ginoux, P., and Ramaswamy, V.: Distribution, transport, and deposition of mineral dust in the Southern Ocean and Antarctica: Contribution of major sources, Journal of Geophysical Research: Atmospheres, 113, https://doi.org/10.1029/2007JD009190, https://agupubs.onlinelibrary.wiley.com/doi/abs/ 10.1029/2007JD009190, 2008.

35 Li, J. and Osada, K.: Preferential settling of elongated mineral dust particles in the atmosphere, Geophysical Research Letters, 34, https://doi.org/10.1029/2007GL030262, https://agupubs.onlinelibrary.wiley.com/doi/ abs/10.1029/2007GL030262, 2007.

Longueville, F. D., Hountondji, Y.-C., Henry, S., and Ozer, P.: What do we know about effects of desert dust on air quality and human health in West Africa compared to other regions?, Science of The Total Environment, 409, 1 – 8, https://doi.org/https://doi.org/10.1016/j.scitotenv.2010.09.025, http://www.sciencedirect.com/science/article/pii/S0048969710009861, 2010.

5 Mahowald, N.: Aerosol Indirect Effect on Biogeochemical Cycles and Climate, Science, 334, 794–796, https://doi.org/10.1126/science.1207374, https://doi.org/10.1126%2Fscience.1207374, 2011.

Mahowald, N., Albani, S., Kok, J. F., Engelstaeder, S., Scanza, R., Ward, D. S., and Flanner, M. G.: The size distribution of desert dust aerosols and its impact on the Earth system, Aeolian Research, 15, 53 – 71, https://doi.org/https://doi.org/10.1016/j.aeolia.2013.09.002, http://www.sciencedirect.com/science/article/pii/S1875963713000736, 2014.

Mahowald, N. M., Baker, A. R., Bergametti, G., Brooks, N., Duce, R. A., Jickells, T. D., Kubilay, N., Prospero, J. M., and Tegen, I.: Atmospheric global dust cycle and iron inputs to the ocean, Global Biogeochemical Cycles, 19, https://doi.org/10.1029/2004GB002402, https://agupubs.onlinelibrary.wiley.com/doi/abs/10.1029/2004GB002402, 2005.

15 Mahowald, N. M., Ballantine, J. A., Feddema, J., and Ramankutty, N.: Global trends in visibility: implications for dust sources, Atmospheric Chemistry and Physics, 7, 3309–3339, https://doi.org/10.5194/acp-7-3309-2007, https://www.atmos-chem-phys.net/7/3309/2007/, 2007.

Mahowald, N. M., Engelstaedter, S., Luo, C., Sealy, A., Artaxo, P., Benitez-Nelson, C., Bonnet, S., Chen, Y., Chuang, P. Y., Cohen, D. D., Dulac, F., Herut, B., Johansen, A. M., Kubilay, N., Losno,

20 R., Maenhaut, W., Paytan, A., Prospero, J. M., Shank, L. M., and Siefert, R. L.: Atmospheric Iron Deposition: Global Distribution, Variability, and Human Perturbations, Annual Review of Marine Science, 1, 245–278, https://doi.org/10.1146/annurev.marine.010908.163727, https://doi.org/10.1146/annurev.marine.010908.163727, pMID: 21141037, 2009.

Marticorena, B. and Bergametti, G.: Modeling the atmospheric dust cycle: 1. Design of a soil-

25 derived dust emission scheme, Journal of Geophysical Research: Atmospheres, 100, 16 415–16 430, https://doi.org/10.1029/95JD00690, https://agupubs.onlinelibrary.wiley.com/doi/abs/10.1029/95JD00690, 1995.

Marticorena, B., Chatenet, B., Rajot, J. L., Traoré, S., Coulibaly, M., Diallo, A., Koné, I., Maman, A., NDiaye, T., and Zakou, A.: Temporal variability of mineral dust concentrations over West Africa: analyses of a pluri-

30 annual monitoring from the AMMA Sahelian Dust Transect, Atmospheric Chemistry and Physics, 10, 8899–8915, https://doi.org/10.5194/acp-10-8899-2010, https://www.atmos-chem-phys.net/10/8899/2010/, 2010.

Marticorena, B., Chatenet, B., Rajot, J. L., Bergametti, G., Deroubaix, A., Vincent, J., Kouoi, A., Schmechtig, C., Coulibaly, M., Diallo, A., Koné, I., Maman, A., NDiaye, T., and Zakou, A.: Mineral dust over west and central Sahel: Seasonal patterns of dry and wet deposition fluxes from a pluriannual sampling (2006–2012),

35 Journal of Geophysical Research: Atmospheres, 122, 1338–1364, https://doi.org/10.1002/2016JD025995, https://agupubs.onlinelibrary.wiley.com/doi/abs/10.1002/2016JD025995, 2017.

Meinshausen, M., Vogel, E., Nauels, A., Lorbacher, K., Meinshausen, N., Etheridge, D. M., Fraser, P. J., Montzka, S. A., Rayner, P. J., Trudinger, C. M., Krummel, P. B., Beyerle, U., Canadell, J. G., Daniel, J. S.,

Enting, I. G., Law, R. M., Lunder, C. R., O'Doherty, S., Prinn, R. G., Reimann, S., Rubino, M., Velders, G. J. M., Vollmer, M. K., Wang, R. H. J., and Weiss, R.: Historical greenhouse gas concentrations for climate modelling (CMIP6), Geoscientific Model Development, 10, 2057–2116, https://doi.org/10.5194/gmd-10-2057-2017, https://gmd.copernicus.org/articles/10/2057/2017/, 2017.

5   Michou, M., Nabat, P., Saint-Martin, D., Bock, J., Decharme, B., Mallet, M., Roehrig, R., Séférian, R., Sénési, S., and Voldoire, A.: Present-Day and Historical Aerosol and Ozone Characteristics in CNRM CMIP6 Simulations, Journal of Advances in Modeling Earth Systems, 12, e2019MS001 816, https://doi.org/10.1029/2019MS001816, https://agupubs.onlinelibrary.wiley.com/doi/abs/10.1029/2019MS001816, e2019MS001816 10.1029/2019MS001816, 2020.

10 Miller, R. L., Cakmur, R. V., Perlwitz, J., Geogdzhayev, I. V., Ginoux, P., Koch, D., Kohfeld, K. E., Prigent, C., Ruedy, R., Schmidt, G. A., and Tegen, I.: Mineral dust aerosols in the NASA Goddard Institute for Space Sciences ModelE atmospheric general circulation model, Journal of Geophysical Research (Atmospheres), 111, D06 208, https://doi.org/https://doi.org/10.1029/2005JD005796, http://adsabs.harvard.edu/abs/2006JGRD..111.6208M, 2006.

15 Monks, P. S., Granier, C., Fuzzi, S., Stohl, A., Williams, M. L., Akimoto, H., Amann, M., Baklanov, A., Baltensperger, U., Bey, I., Blake, N., Blake, R. S., Carslaw, K., Cooper, O. R., Dentener, F., Fowler, D., Fragkou, E., Frost, G. J., Generoso, S., Ginoux, P., Grewe, V., Guenther, A., Hansson, H. C., Henne, S., Hjorth, J., Hofzumahaus, A., Huntrieser, H., Isaksen, I. S. A., Jenkin, M. E., Kaiser, J., Kanakidou, M., Klimont, Z., Kulmala, M., Laj, P., Lawrence, M. G., Lee, J. D., Liousse, C., Maione, M., McFiggans,
20 G., Metzger, A., Mieville, A., Moussiopoulos, N., Orlando, J. J., O'Dowd, C. D., Palmer, P. I., Parrish, D. D., Petzold, A., Platt, U., Pöschl, U., Prévôt, A. S. H., Reeves, C. E., Reimann, S., Rudich, Y., Sellegri, K., Steinbrecher, R., Simpson, D., ten Brink, H., Theloke, J., van der Werf, G. R., Vautard, R., Vestreng, V., Vlachokostas, C., and von Glasow, R.: Atmospheric composition change - global and regional air quality, Atmospheric Environment, 43, 5268–5350, https://doi.org/10.1016/j.atmosenv.2009.08.021, http:
25 //adsabs.harvard.edu/abs/2009AtmEn..43.5268M, 2009.

Nabat, P., Solmon, F., Mallet, M., Kok, J. F., and Somot, S.: Dust emission size distribution impact on aerosol budget and radiative forcing over the Mediterranean region: a regional climate model approach, Atmospheric Chemistry and Physics, 12, 10 545–10 567, https://doi.org/10.5194/acp-12-10545-2012, https://doi.org/10.5194%2Facp-12-10545-2012, 2012.

30 Nousiainen, T.: Optical modeling of mineral dust particles: A review, Journal of Quantitative Spectroscopy and Radiative Transfer, 110, 1261–1279, https://doi.org/10.1016/j.jqsrt.2009.03.002, 2009.

O'Hara, S. L., Clarke, M. L., and Elatrash, M. S.: Field measurements of desert dust deposition in Libya, Atmospheric Environment, 40, 3881 – 3897, https://doi.org/https://doi.org/10.1016/j.atmosenv.2006.02.020, http://www.sciencedirect.com/science/article/pii/S1352231006002305, 2006.

35 Painter, T. H., Barrett, A. P., Landry, C. C., Neff, J. C., Cassidy, M. P., Lawrence, C. R., McBride, K. E., and Farmer, G. L.: Impact of disturbed desert soils on duration of mountain snow cover, Geophysical Research Letters, 34, https://doi.org/10.1029/2007GL030284, https://agupubs.onlinelibrary.wiley.com/doi/abs/10.1029/2007GL030284, 2007.

Perlwitz, J. P., Pérez García-Pando, C., and Miller, R. L.: Predicting the mineral composition of dust aerosols - Part 1: Representing key processes, Atmospheric Chemistry & Physics, 15, 11 593–11 627, https://doi.org/10.5194/acp-15-11593-2015, http://adsabs.harvard.edu/abs/2015ACP....1511593P, 2015.

Peyridieu, S., Chédin, A., Capelle, V., Tsamalis, C., Pierangelo, C., Armante, R., Crevoisier, C., Crépeau, L., Siméon, M., Ducos, F., and Scott, N. A.: Characterisation of dust aerosols in the infrared from IASI and comparison with PARASOL, MODIS, MISR, CALIOP, and AERONET observations, Atmospheric Chemistry and Physics, 13, 6065–6082, https://doi.org/10.5194/acp-13-6065-2013, https://www.atmos-chem-phys.net/13/6065/2013/, 2013.

Piedra, P. G., Llanza, L. R., and Moosmüller, H.: Optical losses of photovoltaic modules due to mineral dust deposition: Experimental measurements and theoretical modeling, Solar Energy, 164, 160 – 173, https://doi.org/https://doi.org/10.1016/j.solener.2018.02.030, http://www.sciencedirect.com/science/article/pii/S0038092X18301634, 2018.

Prenni, A. J., Petters, M. D., Kreidenweis, S. M., Heald, C. L., Martin, S. T., Artaxo, P., Garland, R. M., Wollny, A. G., and Pöschl, U.: Relative roles of biogenic emissions and Saharan dust as ice nuclei in the Amazon basin, Nature Geoscience, 2, 402–405, https://doi.org/https://doi.org/10.1038/ngeo517, http://adsabs.harvard.edu/abs/2009NatGe...2..402P, 2009.

Prospero, J. M. and Nees, R. T.: Impact of the North African drought and El Niño on mineral dust in the Barbados trade winds, Nature, 320, 735–738, https://doi.org/10.1038/320735a0, https://doi.org/10.1038/320735a0, 1986.

Prospero, J. M. and Savoie, D. L.: Effect of continental sources on nitrate concentrations over the Pacific Ocean, Nature, 339, 687–689, https://doi.org/10.1038/339687a0, https://doi.org/10.1038/339687a0, 1989.

Pu, B. and Ginoux, P.: Climatic factors contributing to long-term variations in surface fine dust concentration in the United States, Atmospheric Chemistry & Physics, 18, 4201–4215, https://doi.org/10.5194/acp-18-4201-2018, http://adsabs.harvard.edu/abs/2018ACP....18.4201P, 2018a.

Pu, B. and Ginoux, P.: How reliable are CMIP5 models in simulating dust optical depth?, Atmospheric Chemistry and Physics, 18, 12 491–12 510, https://doi.org/10.5194/acp-18-12491-2018, https://www.atmos-chem-phys.net/18/12491/2018/, 2018b.

Pérez, C., Nickovic, S., Baldasano, J. M., Sicard, M., Rocadenbosch, F., and Cachorro, V. E.: A long Saharan dust event over the western Mediterranean: Lidar, Sun photometer observations, and regional dust modeling, Journal of Geophysical Research: Atmospheres, 111, https://doi.org/10.1029/2005JD006579, https://agupubs.onlinelibrary.wiley.com/doi/abs/10.1029/2005JD006579, 2006.

Pérez, C., Haustein, K., Janjic, Z., Jorba, O., Huneeus, N., Baldasano, J. M., Black, T., Basart, S., Nickovic, S., Miller, R. L., Perlwitz, J. P., Schulz, M., and Thomson, M.: Atmospheric dust modeling from meso to global scales with the online NMMB/BSC-Dust model - Part 1: Model description, annual simulations and evaluation, Atmospheric Chemistry & Physics, 11, 13 001–13 027, https://doi.org/https://doi.org/10.5194/acp-11-13001-2011, http://adsabs.harvard.edu/abs/2011ACP....1113001P, 2011.

Ridley, D. A., Heald, C. L., Kok, J. F., and Zhao, C.: An observationally constrained estimate of global dust aerosol optical depth, Atmospheric Chemistry and Physics, 16, 15 097–15 117, https://doi.org/10.5194/acp-16-15097-2016, https://www.atmos-chem-phys.net/16/15097/2016/, 2016.

Rocha-Lima, A., Martins, J. V., Remer, L. A., Todd, M., Marsham, J. H., Engelstaedter, S., Ryder, C. L., Cavazos-Guerra, C., Artaxo, P., Colarco, P., and Washington, R.: A detailed characterization of the Saharan dust collected during the Fennec campaign in 2011: in situ ground-based and laboratory measurements, Atmospheric Chemistry and Physics, 18, 1023–1043, https://doi.org/10.5194/acp-18-1023-2018, https://www.atmos-chem-phys.net/18/1023/2018/, 2018.

Ryder, C. L., Marenco, F., Brooke, J. K., Estelles, V., Cotton, R., Formenti, P., McQuaid, J. B., Price, H. C., Liu, D., Ausset, P., Rosenberg, P. D., Taylor, J. W., Choularton, T., Bower, K., Coe, H., Gallagher, M., Crosier, J., Lloyd, G., Highwood, E. J., and Murray, B. J.: Coarse-mode mineral dust size distributions, composition and optical properties from AER-D aircraft measurements over the tropical eastern Atlantic, Atmospheric Chemistry and Physics, 18, 17 225–17 257, https://doi.org/10.5194/acp-18-17225-2018, https://www.atmos-chem-phys.net/18/17225/2018/, 2018.

Sayer, A. M., Munchak, L. A., Hsu, N. C., Levy, R. C., Bettenhausen, C., and Jeong, M.-J.: MODIS Collection 6 aerosol products: Comparison between Aqua's e-Deep Blue, Dark Target, and "merged" data sets, and usage recommendations, Journal of Geophysical Research: Atmospheres, 119, 13,965–13,989, https://doi.org/10.1002/2014JD022453, https://agupubs.onlinelibrary.wiley.com/doi/abs/10.1002/2014JD022453, 2014.

Scanza, R. A., Mahowald, N., Ghan, S., Zender, C. S., Kok, J. F., Liu, X., Zhang, Y., and Albani, S.: Modeling dust as component minerals in the Community Atmosphere Model: development of framework and impact on radiative forcing, Atmospheric Chemistry & Physics, 15, 537–561, https://doi.org/https://doi.org/10.5194/acp-15-537-2015, 2015.

Schulz, M., Balkanski, Y. J., Guelle, W., and Dulac, F.: Role of aerosol size distribution and source location in a three-dimensional simulation of a Saharan dust episode tested against satellite-derived optical thickness, Journal of Geophysical Research: Atmospheres, 103, 10 579–10 592, https://doi.org/10.1029/97JD02779, https://agupubs.onlinelibrary.wiley.com/doi/abs/10.1029/97JD02779, 1998.

Schulz, M., Cozic, A., and Szopa, S.: LMDzT-INCA dust forecast model developments and associated validation efforts, IOP Conference Series: Earth and Environmental Science, 7, 012 014, https://doi.org/https://doi.org/10.1088/1755-1307/7/1/012014, 2009.

Schulz, M., Prospero, J. M., Baker, A. R., Dentener, F., Ickes, L., Liss, P. S., Mahowald, N. M., Nickovic, S., García-Pando, C. P., Rodríguez, S., Sarin, M., Tegen, I., and Duce, R. A.: Atmospheric Transport and Deposition of Mineral Dust to the Ocean: Implications for Research Needs, Environmental Science and Technology, 46, 10 390–10 404, https://doi.org/10.1021/es300073u, 2012.

Seinfeld, J. and Pandis, S.: Atmospheric chemistry and physics: from air pollution to climate change, A Wiley interscience publication, Wiley, https://books.google.fr/books?id=lK8PAQAAMAAJ, 1998.

Sellar, A. A., Jones, C. G., Mulcahy, J. P., Tang, Y., Yool, A., Wiltshire, A., O'Connor, F. M., Stringer, M., Hill, R., Palmieri, J., Woodward, S., de Mora, L., Kuhlbrodt, T., Rumbold, S. T., Kelley, D. I., Ellis, R., Johnson,

C. E., Walton, J., Abraham, N. L., Andrews, M. B., Andrews, T., Archibald, A. T., Berthou, S., Burke, E., Blockley, E., Carslaw, K., Dalvi, M., Edwards, J., Folberth, G. A., Gedney, N., Griffiths, P. T., Harper, A. B., Hendry, M. A., Hewitt, A. J., Johnson, B., Jones, A., Jones, C. D., Keeble, J., Liddicoat, S., Morgenstern, O., Parker, R. J., Predoi, V., Robertson, E., Siahaan, A., Smith, R. S., Swaminathan, R., Woodhouse, M. T., Zeng, G., and Zerroukat, M.: UKESM1: Description and Evaluation of the U.K. Earth System Model, Journal of Advances in Modeling Earth Systems, 11, 4513–4558, https://doi.org/10.1029/2019MS001739, https://agupubs.onlinelibrary.wiley.com/doi/abs/10.1029/2019MS001739, 2019.

Shaffer, G., Olsen, S. M., and Pedersen, J. O. P.: Long-term ocean oxygen depletion in response to carbon dioxide emissions from fossil fuels, Nature Geoscience, 2, 105, https://doi.org/10.1038/ngeo420, 2009.

Shao, Y.: A model for mineral dust emission, Journal of Geophysical Research: Atmospheres, 106, 20 239–20 254, https://doi.org/10.1029/2001JD900171, https://agupubs.onlinelibrary.wiley.com/doi/abs/10.1029/2001JD900171, 2001.

Shao, Y.: Simplification of a dust emission scheme and comparison with data, Journal of Geophysical Research: Atmospheres, 109, https://doi.org/10.1029/2003JD004372, https://agupubs.onlinelibrary.wiley.com/doi/abs/10.1029/2003JD004372, 2004.

Shao, Y.: Physics and Modelling Wind Erosion, vol. 23, Springer-Werlag, 2008.

Shao, Y. and Dong, C.: A review on East Asian dust storm climate, modelling and monitoring, Global and Planetary Change, 52, 1–22, https://doi.org/10.1016/j.gloplacha.2006.02.011, https://doi.org/10.1016/j.gloplacha.2006.02.011, 2006.

Shao, Y., Wyrwoll, K.-H., Chappell, A., Huang, J., Lin, Z., McTainsh, G. H., Mikami, M., Tanaka, T. Y., Wang, X., and Yoon, S.: Dust cycle: An emerging core theme in Earth system science, Aeolian Research, 2, 181–204, https://doi.org/10.1016/j.aeolia.2011.02.001, https://doi.org/10.1016%2Fj.aeolia.2011.02.001, 2011.

Sharma, D. and Miller, R. L.: Revisiting the observed correlation between weekly averaged Indian monsoon precipitation and Arabian Sea aerosol optical depth, Geophysical Research Letters, 44, 10,006–10,016, https://doi.org/10.1002/2017GL074373, https://agupubs.onlinelibrary.wiley.com/doi/abs/10.1002/2017GL074373, 2017.

Shindell, D. T., Lamarque, J. F., Schulz, M., Flanner, M., Jiao, C., Chin, M., Young, P. J., Lee, Y. H., Rotstayn, L., Mahowald, N., Milly, G., Faluvegi, G., Balkanski, Y., Collins, W. J., Conley, A. J., Dalsoren, S., Easter, R., Ghan, S., Horowitz, L., Liu, X., Myhre, G., Nagashima, T., Naik, V., Rumbold, S. T., Skeie, R., Sudo, K., Szopa, S., Takemura, T., Voulgarakis, A., Yoon, J. H., and Lo, F.: Radiative forcing in the ACCMIP historical and future climate simulations, Atmospheric Chemistry and Physics, 13, 2939–2974, https://doi.org/10.5194/acp-13-2939-2013, https://doi.org/10.5194%2Facp-13-2939-2013, 2013.

Solomos, S., Kallos, G., Kushta, J., Astitha, M., Tremback, C., Nenes, A., and Levin, Z.: An integrated modeling study on the effects of mineral dust and sea salt particles on clouds and precipitation, Atmospheric Chemistry and Physics, 11, 873–892, https://doi.org/10.5194/acp-11-873-2011, https://acp.copernicus.org/articles/11/873/2011/, 2011.

Strong, J. D. O., Vecchi, G. A., and Ginoux, P.: The Response of the Tropical Atlantic and West African Climate to Saharan Dust in a Fully Coupled GCM, Journal of Climate, 28, 7071–7092, https://doi.org/10.1175/JCLI-D-14-00797.1, /brokenurl#https://doi.org/10.1175/JCLI-D-14-00797.1, 2015.

Séférian, R., Nabat, P., Michou, M., Saint-Martin, D., Voldoire, A., Colin, J., Decharme, B., Delire, C., Berthet, S., Chevallier, M., Sénési, S., Franchisteguy, L., Vial, J., Mallet, M., Joetzjer, E., Geoffroy, O., Guérémy, J.-F., Moine, M.-P., Msadek, R., Ribes, A., Rocher, M., Roehrig, R., Salas-y Mélia, D., Sanchez, E., Terray, L., Valcke, S., Waldman, R., Aumont, O., Bopp, L., Deshayes, J., Éthé, C., and Madec, G.: Evaluation of CNRM Earth-System model, CNRM-ESM 2-1: role of Earth system processes in present-day and future climate, Journal of Advances in Modeling Earth Systems, 11, 4182– 4227, https://doi.org/10.1029/2019MS001791, 2019.

Tang, M., Cziczo, D. J., and Grassian, V. H.: Interactions of Water with Mineral Dust Aerosol: Water Adsorption, Hygroscopicity, Cloud Condensation, and Ice Nucleation, Chemical Reviews, 116, 4205– 4259, https://doi.org/10.1021/acs.chemrev.5b00529, https://doi.org/10.1021/acs.chemrev.5b00529, pMID: 27015126, 2016.

Tang, M., Huang, X., Lu, K., Ge, M., Li, Y., Cheng, P., Zhu, T., Ding, A., Zhang, Y., Gligorovski, S., Song, W., Ding, X., Bi, X., and Wang, X.: Heterogeneous reactions of mineral dust aerosol: implications for tropospheric oxidation capacity, Atmospheric Chemistry and Physics, 17, 11 727–11 777, https://doi.org/10.5194/acp-17-11727-2017, https://www.atmos-chem-phys.net/17/11727/2017/, 2017.

Taylor, K. E.: Summarizing multiple aspects of model performance in a single diagram, Journal of Geophysical Research: Atmospheres, 106, 7183–7192, https://doi.org/10.1029/2000jd900719, https://doi.org/10.1029%2F2000jd900719, 2001.

Tegen, I. and Fung, I.: Modeling of mineral dust in the atmosphere: Sources, transport, and optical thickness, Journal of Geophysical Research, 99, 22 897, https://doi.org/https://doi.org/10.1029/94jd01928, 1994.

Tegen, I., Harrison, S. P., Kohfeld, K., Prentice, I. C., Coe, M., and Heimann, M.: Impact of vegetation and preferential source areas on global dust aerosol: Results from a model study, Journal of Geophysical Research: Atmospheres, 107, AAC 14–1–AAC 14–27, https://doi.org/10.1029/2001JD000963, https://agupubs.onlinelibrary.wiley.com/doi/abs/10.1029/2001JD000963, 2002.

Timmreck, C. and Schulz, M.: Significant dust simulation differences in nudged and climatological operation mode of the AGCM ECHAM, Journal of Geophysical Research: Atmospheres, 109, n/a–n/a, https://doi.org/10.1029/2003jd004381, https://doi.org/10.1029%2F2003jd004381, 2004.

van der Does, M., Knippertz, P., Zschenderlein, P., Harrison, R. G., and Stuut, J.-B. W.: The mysterious long-range transport of giant mineral dust particles, Science Advances, 4, eaau2768, https://doi.org/10.1126/sciadv.aau2768, https://doi.org/10.1126/sciadv.aau2768, 2018.

Vincent, J., Laurent, B., Losno, R., Bon Nguyen, E., Roullet, P., Sauvage, S., Chevaillier, S., Coddeville, P., Ouboulmane, N., di Sarra, A. G., Tovar-Sánchez, A., Sferlazzo, D., Massanet, A., Triquet, S., Morales Baquero, R., Fornier, M., Coursier, C., Desboeufs, K., Dulac, F., and Bergametti, G.: Variability of mineral dust deposition in the western Mediterranean basin and south-east of France, Atmospheric Chemistry and

Yu, Y., Kalashnikova, O. V., Garay, M. J., and Notaro, M.: Climatology of Asian dust activation and transport potential based on MISR satellite observations and trajectory analysis, Atmospheric Chemistry and Physics, 19, 363–378, https://doi.org/10.5194/acp-19-363-2019, https://www.atmos-chem-phys.net/19/363/2019/, 2019.

Zender, C. S., Bian, H., and Newman, D.: Mineral Dust Entrainment and Deposition (DEAD) model: Description and 1990s dust climatology, Journal of Geophysical Research (Atmospheres), 108, 4416, https://doi.org/https://doi.org/10.1029/2002JD002775, http://adsabs.harvard.edu/abs/2003JGRD..108. 4416Z, 2003.